energies

MDPI

Article

Investigation on Tuning Power–Frequency Droop for Improved Grid–Forming Inverter and Synchronous Generator Transient Load Sharing

Jan Westman * and Ramtin Hadidi

Department of Electrical and Computer Engineering, Clemson University, Charleston, SC 29405, USA; rhadidi@clemson.edu

* Correspondence: jwestma@clemson.edu

Abstract: Poor transient load sharing has been observed during the parallel operation of synchronous generators (SGs) and droop-controlled grid-forming (GFM) inverter-based resources (IBRs) in islanded microgrids. This can result in overcurrent protections, causing the inverters to trip, which leads to the collapse of voltage and frequency. In this article, small-signal analysis supported by electromagnetic transients (EMTs) simulation is performed on a detailed model of a microgrid containing IBRs and an SG to identify underdamped modes and their sensitivities to the power–frequency (P-F) droop parameter. Further EMT simulation of a more complex microgrid model with multiple GFM IBRs and SGs is performed to determine whether trends identified from the modal analysis extend to cases where the number of SGs in operation may vary. The objective is to investigate the effectiveness of tuning this parameter to reduce the likelihood of overcurrents in response to load and generation disturbances. The work uncovers both fast and slow modes of concern. Primarily, the findings show that increasing the P-F droop value improves the damping of the slower mode while degrading the damping of the faster mode, leading to an upper limit on the damping improvement of the GFM IBR output current. In EMT simulations of the more complex microgrid, the greatest damping improvement still exhibits significant maximum overshoot. Furthermore, the optimal value of the P-F droop parameter is sensitive to the number of SGs in operation. The conclusion is that tuning the P-F droop parameter is not an effective means to avoid the overcurrent tripping of GFM IBRs during response to large load or generation disturbances when operating in parallel to SGs in islanded microgrids.

Keywords: grid-forming inverters; small-signal analysis; synchronous generators; transient load sharing

Citation: Westman, J.; Hadidi, R. Investigation on Tuning Power–Frequency Droop for Improved Grid–Forming Inverter and Synchronous Generator Transient Load Sharing. *Energies* **2023**, *16*, 6758. https://doi.org/10.3390/en16186758

Academic Editor: Ahmed Abu-Siada

Received: 23 August 2023
Revised: 15 September 2023
Accepted: 18 September 2023
Published: 21 September 2023

1. Introduction

Implementing microgrids capable of independent operation can be a solution to provide a reliable electricity supply. This particularly applies to remote locations where a grid connection is unavailable or where service interruptions are frequent. Under these circumstances, integrating renewable energy resources coupled with energy storage reduces emissions and fuel costs, which are otherwise incurred by operating conventional synchronous generators (SGs) [1]. The already low amount of inertia in these power systems is thus further reduced if SGs are shutdown to prevent operating below minimum load, which can cause operational problems for these devices [2]. This may occur during periods of high renewable energy availability and increases the likelihood of frequency instability [3]. To address this issue, applying the grid-forming (GFM) droop control of inverter-based resources (IBRs) in parallel to SGs has been shown to improve the frequency response to load and generation disturbances in [1,4,5]. Full-scale demonstrations of such scenarios are available in [6,7].

Power–frequency droop control is a mature and widely used strategy for the load sharing of grid-forming inverters in standalone power systems. It is summarized by the following equation, which provides the frequency reference ω_i of the droop-controlled inverter

$$\omega_i = \omega_i^* + d_{p,i}(P_i^* - P_i), \tag{1}$$

where ω_i^* is a frequency setpoint (fixed or set by a secondary controller), P_i^* is an active power setpoint (fixed or set by a secondary controller), and P_i is the measured active power output of the inverter. A common method of selecting the droop slope $d_{p,i}$ was presented in [8], which was given as

$$d_{p,i} = \frac{\omega_{min} - \omega_{max}}{P_{max,i} - P_{min,i}}. \tag{2}$$

Here, $P_{max,i}$ and $P_{min,i}$ are the maximum and minimum output active power of the ith inverter, respectively, and ω_{max} and ω_{min} represent the range of allowable operating frequencies of the microgrid. The authors of [4] provided operational frequency bands of international grid codes. The range of maximum positive frequency deviations spanned from 0.016 pu to 0.04 pu and maximum negative frequency deviations spanned from −0.016 pu to −0.06 pu. Since the denominator of (2) is 2.0 pu for a four-quadrant device, a range of typical power–frequency droop slopes would be from 0.016 pu/pu to 0.05 pu/pu. However, both smaller and larger droop slopes were often used in the works reviewed for this manuscript. This was observed from a survey of power–frequency droop values, converted to pu/pu, which are documented in Table 1.

Table 1. Power–frequency droop slopes from cited references.

References	Droops (pu/pu)
[9–11]	0.01
[1,12]	0.05
[3]	0.008–0.2
[5]	0.01, 0.05
[6]	0.083
[7]	0.04
[13]	0.017
[14]	0.0005–0.01
[15]	0.0265
[16]	0.02
[17]	0.01–0.092
[18]	0.017, 0.033, 0.066

In [18], it was shown that the GFM IBRs initially picked up the majority of an abrupt load increase when operating in parallel to an SG. The transient load on the inverter significantly exceeded its post-disturbance steady state load. This phenomenon could trigger the collapse of a microgrid as successive trips of GFM IBRs occur due to the activation of protection thresholds. Such scenarios were demonstrated in [9,10]. Existing efforts addressing this problem proposed control schemes to limit the IBR output power during transient conditions. This led to three forms of current-limiting controls: (1) the utilization of current reference limits in a multi-loop GFM implementation [19]; (2) switching from voltage regulation to current regulation (i.e., grid following (GFL) operation) when the overcurrent occurred [20]; and (3) virtual impedance current limiting, which effectively reduced the IBR voltage behind an impedance [13]. Alternatives to these approaches attempted to dynamically modify the power–frequency relationship of the droop control [10,11]. While these efforts made progress toward improving the reliability of microgrids with GFM IBRs and synchronous machines, they focused on developing additional control schemes added on top of the GFM P-F droop control strategy. In contrast, the work in this paper focused on studying how the P-F droop control itself impacted the damping of the output current of a GFM IBR when operated in parallel to synchronous generators in islanded microgrids.

Other works investigated the damping of important modes in power systems containing droop-controlled GFM IBRs and SGs. Generally, small-signal analysis was performed on reduced-order models to qualitatively describe the interaction of these resources as in [5,12,21,22]. These works focused on the frequency response and the results consistently showed that an increased penetration of GFM IBRs improved the damping of modes observed in the reduced-order models. However, these analyses were limited to slow-moving modes associated with the SG rotor speeds. This limitation was highlighted in [12], where EMT simulation revealed a faster underdamped mode when the GFM IBR penetration was high. Thus, it was unclear whether the damping of faster modes associated with the GFM IBR output current would also be improved and how that trend would be sensitive to the P-F droop parameter. In contrast, small-signal analyses of higher-order microgrid models using a rotating reference frame (RRF) approach were performed in [14,23,24], where the authors presented the response of the dominant system modes to variations in the P-F droop parameter. However, these microgrid models did not include synchronous generators. Finally, the authors in [25,26] studied microgrids containing SGs. They also explored the sensitivity of modes to the GFM IBR P-F droop slope. However, they did not vary other important parameters related to SG and GFM IBR interaction such as the SG inertia or the number of SGs in operation. Additionally, these works assumed SG inertia constants of 5.6 s and 3.5 s, respectively, which are quite large for SGs found in microgrid applications (see 0.4 s cited in [1] and 0.345 s and 1.86 s cited in [27] from real equipment data).

The work in this paper contributed to research into GFM IBR and SG interaction for the improvement of transient load sharing by performing a small-signal analysis of a detailed, mixed-source microgrid model. EMT simulations of the microgrid model were performed to support the observations from the small-signal model. Additional simulation was performed for a more complex microgrid model to determine if the results extend to microgrids with multiple SGs and GFM IBRs. The small-signal analysis and simulations addressed the limitations and shortcomings discussed above by performing a sensitivity analysis of the modes to the P-F droop parameter and SG inertia. The results of this investigation provided valuable insights regarding how the P-F droop parameter affected transient load sharing between these devices. The damping of the GFM IBR output current response was found to be highly sensitive to the P-F droop parameter. However, improvements in the damping achieved by tuning the parameter were limited due to the increasing participation of a faster underdamped mode as the P-F droop parameter was increased. Furthermore, in the microgrid with multiple SGs, the optimal P-F droop value depended on the number of SGs in operation, which would add complexity to any potential tuning algorithm. For these reasons, the investigation concluded that tuning the P-F droop parameter was not an effective means to mitigate poor transient load sharing in low-inertia islanded microgrids.

2. Small-Signal Modeling of a Mixed-Source Microgrid

The transient overload phenomenon involves a large-signal disturbance where a structural change to the microgrid occurs. This disturbance can be the disconnection of an existing distributed energy resource (DER) (generation trip) or the re-connection of a large load (load acceptance). The results are significant changes in the steady state outputs of the DER and a new microgrid operating point. Linearizations of nonlinear models are generally valid only in a small region around an operating point. However, the size of this region depends on the required approximations. Thus, a change in operating point is not guaranteed to significantly impact the locations of system modes. Therefore, small-signal analyses can be applied to the large-signal phenomenon in some cases.

Results from prior works suggested that small-signal models could accurately reproduce responses to large-signal stimuli. The responses to significant load disturbances predicted using the small-signal RRF models of multi-IBR microgrids were validated against laboratory-scale experimental test set-ups in [14,15]. Furthermore, in [16,28], varia-

tion in the operating point around which small-signal models were linearized produced minimal changes in the system modes. Finally, in [29], variation in the DER loading of a mixed-source microgrid had a small effect on modes of interest and did not substantially change the sensitivities of those modes to variation in the P-F droop parameter. Leveraging these findings as justification, a small-signal model of a microgrid , illustrated in Figure 1, was developed in order to perform sensitivity analyses to the P-F droop parameter and SG inertia constant.

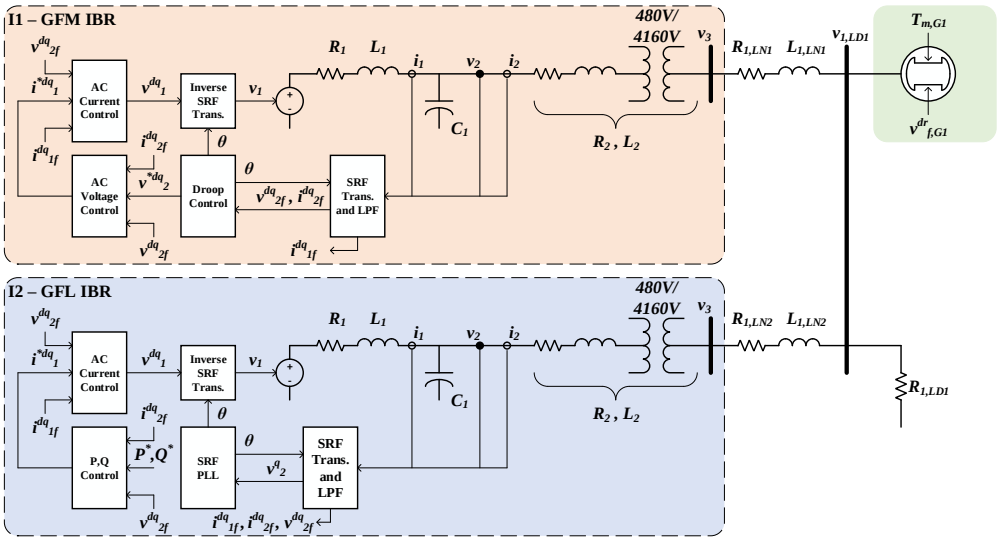

Figure 1. Diagram of the single Grid-Forming (GFM) Inverter Based Resource (IBR) microgrid. GFM IBR model is highlighted in red and Grid-Following IBR model is highlighted in blue. Refer to Section 2.1.2 through Section 2.1.4 for the GFM IBR controller subsystems. Refer to Section 2.2.1 through Section 2.2.3 for the GFL IBR controller subsystems.

The system in Figure 1 was composed of three DERs: an SG, a three-phase GFM IBR, and a three-phase grid following (GFL) IBRs. The differential and algebraic equations describing the model dynamics were linearized and per unitized on the system base to form the small-signal model. A nonlinear, EMT model of this microgrid was created using Simscape Electrical Specialized Power System toolbox in Matlab/Simulink. The EMT model was used to simulate a load acceptance scenario for comparison with the modal analysis results. The power system model simulation type was discrete with a time step of 50 µs, while the overall model used the default fixed-step solver, also with a 50 µs time step. The interconnecting impedances and resistive load were balanced, which facilitated the use of the RRF modeling approach. The following subsections present the small-signal model of this system, which will be referred to as the single GFM IBR microgrid for brevity in distinguishing this model from a second microgrid model presented in Section 3. Validation of the small-signal model is presented in Section 4.1.

In the following sections, the subscript 0 was used to denote the value of a variable at the operating point at which the model was linearized. A bar was used to denote a per unitized variable or parameter on the system base, which was 2.5 MVA, 4160 V, and 60 Hz. The subscript b denoted the system base value of a quantity such as power, voltage, frequency, impedance, and admittance. The model parameters are available in Table A1 of Appendix A.

2.1. Grid-Forming Inverter Model

The GFM IBR model, denoted as I1 in Figure 1, was representative of a battery energy storage system and was composed of an LCL filter, an average value model of a two-level voltage source converter, and a fixed DC voltage source, which neglected the DC subsystem dynamics. In [12], the authors found that the adequate sizing of the DC bus capacitor

buffered the DC voltage against short-time AC-side output disturbances and thus, this was considered a suitable simplification.

2.1.1. LCL Filter

The LCL filter incorporated a smaller inductor at the inverter terminals followed by a shunt capacitor and then a second, larger inductor, which was consistent with the configuration recommended for multi-loop GFM droop control, as found in [17]. Finally, a step-up transformer connected the GFM IBR AC subsystem to the medium voltage network. The second inductor and step-up transformer were combined and modeled as a series RL circuit with series resistance $\bar{R}_{2,I1}$ and inductance $\bar{L}_{2,I1}$. The dynamic equations describing the LCL filter dynamics were

$$\frac{\bar{L}_{1,I1}}{\omega_b}\frac{d\Delta\bar{i}^{dq}_{1,I1}}{dt} = (\bar{\omega}_0\bar{L}_{1,I1}G_{ROT} - \bar{R}_{1,I1})\Delta\bar{i}^{dq}_{1,I1} + \Delta\bar{v}^{dq}_{1,I1} - \Delta\bar{v}^{dq}_{2,I1}\,, \tag{3}$$

$$\frac{\bar{C}_{1,I1}}{\omega_b}\frac{d\Delta\bar{v}^{dq}_{2,I1}}{dt} = \bar{\omega}_0\bar{C}_{1,I1}G_{ROT}\Delta\bar{v}^{dq}_{2,I1} + \Delta\bar{i}^{dq}_{1,I1} - \Delta\bar{i}^{dq}_{2,I1}\,, \tag{4}$$

and

$$\frac{\bar{L}_{2,I1}}{\omega_b}\frac{d\Delta\bar{i}^{dq}_{2,I1}}{dt} = (\bar{\omega}_0\bar{L}_{2,I1}G_{ROT} - \bar{R}_{2,I1})\Delta\bar{i}^{dq}_{2,I1} + \Delta\bar{v}^{dq}_{2,I1} - \Delta\bar{v}^{dq}_{3,I1}\,, \tag{5}$$

where

$$G_{ROT} = \begin{bmatrix} 0 & 1 \\ -1 & 0 \end{bmatrix}. \tag{6}$$

The superscript dq denotes the vector of direct (d) and quadrature (q) components of a rotating vector obtained from a three-phase set of stationary reference frame variables by the following transformation:

$$f^{dq} = \begin{bmatrix} cos(\omega t) & cos(\omega t - \frac{2\pi}{3}) & cos(\omega t + \frac{2\pi}{3}) \\ -sin(\omega t) & -sin(\omega t - \frac{2\pi}{3}) & -sin(\omega t + \frac{2\pi}{3}) \end{bmatrix} \begin{bmatrix} f_{as} \\ f_{bs} \\ f_{cs} \end{bmatrix}, \tag{7}$$

where ωt is the angular deflection between the stationary as axis and the rotating vector when the d-component is non-zero and the q-component is zero. Thus, ω is the angular velocity of the rotating vector. Note that with the definition of the RRF in (7), the d-axis is aligned with the as-axis when ωt is zero and the q-axis leads the d-axis by 90 degrees.

2.1.2. Inner Loop Current Control

The inner loop current controller regulated the current flowing to the LCL filter capacitor by utilizing proportional–integral (PI) control and feedforward decoupling terms. This allowed the GFM IBR to control the AC voltage across the capacitor. The RRF terminal voltage references produced by the inner loop current controller were equated to the physical RRF inverter terminal voltages. This was feasible by neglecting the DC bus dynamics and assuming an ideal operation of the two-level voltage source converter pulse width modulation (PWM) control. The result was the following differential and algebraic equations defining the current controller:

$$\Delta\bar{v}^{dq}_{1,I1} = \Delta\bar{v}^{dq}_{2f,I1} + Y_b k_{pi,I1}(\Delta\bar{i}^{*,dq}_{1,I1} - \Delta\bar{i}^{dq}_{1f,I1}) + \bar{U}^{dq}_{i,I1} - \bar{\omega}_b\bar{L}_{1,I1}G_{ROT}\Delta\bar{i}^{dq}_{1f,I1}\,, \tag{8}$$

$$\frac{d\Delta\bar{i}^{dq}_{1f,I1}}{dt} = \omega_{c1,I1}(\Delta\bar{i}^{dq}_{1,I1} - \Delta\bar{i}^{dq}_{1f,I1})\,, \tag{9}$$

$$\frac{d\Delta\bar{v}^{dq}_{2f,I1}}{dt} = \omega_{c1,I1}(\Delta\bar{v}^{dq}_{2,I1} - \Delta\bar{v}^{dq}_{2f,I1})\,, \tag{10}$$

and

$$\frac{d\Delta\bar{U}_{i,I1}^{dq}}{dt} = Y_b k_{ii,I1}(\Delta\bar{\vec{i}}_{1,I1}^{*dq} - \Delta\bar{\vec{i}}_{1f,I1}^{dq}) \,. \tag{11}$$

The voltage and current low-pass-filter cutoff frequency $\omega_{c1,I1}$ was chosen to be a decade lower than a hypothetical switching frequency of 4 kHz, creating a realistic upper limit on the bandwidth of the current controller. The PI controller gains were tuned experimentally, starting with k_{pi} to obtain a rise time on the order of a few ms and good stability margin.

2.1.3. Outer Loop Voltage Control

The outer loop voltage controller used PI control and feedforward decoupling terms to synthesize the references for the inner loop current controller based on the LCL filter capacitor voltage error. The equations describing this controller were

$$\Delta\bar{\vec{i}}_{1,I1}^{*dq} = Z_b k_{pv,I1}(\Delta\bar{v}_{2,I1}^{*dq} - \Delta\bar{v}_{2f,I1}^{dq}) + \Delta\bar{U}_{v,I1}^{dq} - \bar{\omega}_b\bar{C}_{1,I1}G_{ROT}\Delta\bar{v}_{2fq,I1} + \Delta\bar{\vec{i}}_{2f,I1}^{dq} \,, \tag{12}$$

$$\frac{d\Delta\bar{\vec{i}}_{2f,I1}^{dq}}{dt} = \omega_{c1,I1}(\Delta\bar{\vec{i}}_{2,I1}^{dq} - \Delta\bar{\vec{i}}_{2f,I1}^{dq}) \,, \tag{13}$$

and

$$\frac{d\Delta\bar{U}_{v,I1}^{dq}}{dt} = Z_b k_{iv,I1}(\Delta\bar{v}_{2,I1}^{*dq} - \Delta\bar{v}_{2f,I1}^{dq}) \,. \tag{14}$$

2.1.4. Active and Reactive Power Droop Control

Droop control was employed in order to maintain synchronism and achieve proportional steady-state active and reactive power load sharing with the SG. The linearized droop control equations were

$$\Delta\bar{\omega}_{I1} = \Delta\bar{\omega}_{I1}^{*} + \bar{d}_{p,I1}(\Delta\bar{P}_{I1}^{*} - \Delta\bar{P}_{f,I1}) \,, \tag{15}$$

$$\Delta\bar{v}_{2,I1}^{*dq} = \begin{bmatrix} \Delta\bar{v}_{I1}^{*} - \bar{d}_{q,I1}\Delta\bar{Q}_{f,I1} \\ 0 \end{bmatrix}, \tag{16}$$

$$\frac{d\Delta\bar{P}_{f,I1}}{dt} = \omega_{c2,I1}(\Delta\bar{P}_{I1} - \Delta\bar{P}_{f,I1}) \,, \tag{17}$$

$$\Delta\bar{P}_{I1} = (\bar{\vec{i}}_{2f,I1,0}^{dq})^T\Delta\bar{v}_{2f,I1}^{dq} + (\bar{v}_{2f,I1,0}^{dq})^T\Delta\bar{\vec{i}}_{2f,I1}^{dq} \,, \tag{18}$$

$$\frac{d\Delta\bar{Q}_{f,I1}}{dt} = \omega_{c2,I1}(\Delta\bar{Q}_{I1} - \Delta\bar{Q}_{f,I1}) \,, \tag{19}$$

and

$$\Delta\bar{Q}_{I1} = (\bar{\vec{i}}_{2f,I1,0}^{dq})^T G_{ROT}\Delta\bar{v}_{2f,I1}^{dq} - (\bar{v}_{2f,I1,0}^{dq})^T G_{ROT}\Delta\bar{\vec{i}}_{2f,I1}^{dq}. \tag{20}$$

The low-pass filtering of the measured active power was important for avoiding fast frequency deviations and eliminating measurement noise, as discussed in [28]. Additionally, it was found in [28] that the active power measurement low-pass filter significantly changed the behavior of the GFM IBR. Thus, including this model detail and selecting an appropriate cutoff frequency (see [28]) was necessary for obtaining realistic models of GFM IBRs.

2.2. Grid Following Inverter Model

The GFL IBR model, denoted as I2 in Figure 1, was representative of a renewable energy resource with variable output such as a solar/photovoltaic (PV) plant. Similar to the GFM IBR model, it was composed of an LCL filter, an average value two-level voltage source converter model, and a fixed DC voltage source. The principle difference from the GFM IBR was the outer control loops and parameter values. For brevity, the LCL

filter equations were omitted from the following subsections as these may be obtained by substituting the GFM IBR subscript I1 for the GFL IBR subscript I2 in (3)–(5).

Note that trigonometric terms appeared in the GFL IBR control equations that were absent from the GFM IBR control equations. This was due to using the GFM IBR RRF as the common RRF for physical system quantities, while other device control system quantities were established in independent RRFs. Thus, linearized frame–frame transformations were required to relate physical system quantities to their counterparts in the RRFs established by other device control systems. More detailed explanations were provided in [14,15]. The linearized forward transformation was

$$\Delta f^{dq,c} = \begin{bmatrix} cos(\delta_{c,0}) & sin(\delta_{c,0}) \\ -sin(\delta_{c,0}) & cos(\delta_{c,0}) \end{bmatrix} \Delta f^{dq} + \begin{bmatrix} -f_0^d sin(\delta_{c,0}) + f_0^q cos(\delta_{c,0}) \\ -f_0^d cos(\delta_{c,0}) - f_0^q sin(\delta_{c,0}) \end{bmatrix} \Delta\delta_c \tag{21}$$

and the inverse was

$$\Delta f^{dq} = \begin{bmatrix} cos(\delta_{c,0}) & -sin(\delta_{c,0}) \\ sin(\delta_{c,0}) & cos(\delta_{c,0}) \end{bmatrix} \Delta f^{dq,c} + \begin{bmatrix} -f_0^{d,c} sin(\delta_{c,0}) - f_0^{q,c} cos(\delta_{c,0}) \\ f_0^{d,c} cos(\delta_{c,0}) - f_0^{q,c} sin(\delta_{c,0}) \end{bmatrix} \Delta\delta_c \tag{22}$$

where

$$\frac{d}{dt}\Delta\delta_c = \omega_b(\Delta\omega_c - \Delta\omega_{I1}) \,. \tag{23}$$

The superscript c indicates the physical quantity counterpart in the device controller RRF and the subscript 0 indicates the quantity at the steady-state operating point.

2.2.1. Inner Loop Current Control

The inner loop current controller of the GFL IBR was identical to the GFM IBR. The PI controller and low-pass filter equations, integrated with the frame–frame transformations, were

$$\Delta\bar{v}_{1,I2}^{dq} = \begin{bmatrix} cos(\delta_{I2,0}) & -sin(\delta_{I2,0}) \\ sin(\delta_{I2,0}) & cos(\delta_{I2,0}) \end{bmatrix} \Delta\bar{v}_{1,I2}^{*dq} + \begin{bmatrix} -\bar{v}_{1,I2,0}^{*d} sin(\delta_{I2,0}) - \bar{v}_{1,I2,0}^{*q} cos(\delta_{I2,0}) \\ \bar{v}_{1,I2,0}^{*d} cos(\delta_{I2,0}) - \bar{v}_{1,I2,0}^{*q} sin(\delta_{I2,0}) \end{bmatrix} \Delta\delta_{I2} \,, \tag{24}$$

$$\Delta\bar{v}_{1,I2}^{*dq} = \Delta\bar{v}_{2f,I2}^{dq} + Y_b k_{pi,I2}(\Delta\bar{i}_{1,I2}^{*,dq} - \Delta\bar{i}_{1f,I2}^{dq}) + \bar{U}_{i,I2}^{dq} - \bar{\omega}_b \bar{L}_{1,I2} G_{ROT} \Delta\bar{i}_{1f,I2}^{dq} \,, \tag{25}$$

$$\frac{d\Delta\bar{i}_{1f,I2}^{dq}}{dt} = \omega_{c1,I2}\left(\begin{bmatrix} cos(\delta_{I2,0}) & sin(\delta_{I2,0}) \\ -sin(\delta_{I2,0}) & cos(\delta_{I2,0}) \end{bmatrix} \Delta\bar{i}_{1,I2}^{dq} + \begin{bmatrix} -\bar{i}_{1,I2,0}^{d} sin(\delta_{I2,0}) + \bar{i}_{1,I2,0}^{q} cos(\delta_{I2,0}) \\ -\bar{i}_{1,I2,0}^{d} cos(\delta_{I2,0}) - \bar{i}_{1,I2,0}^{q} sin(\delta_{I2,0}) \end{bmatrix} \Delta\delta_{I2} - \Delta\bar{i}_{1f,I2}^{dq} \right) \,, \tag{26}$$

$$\frac{d\Delta\bar{v}_{2f,I2}^{dq}}{dt} = \omega_{c2,I2}\left(\begin{bmatrix} cos(\delta_{I2,0}) & sin(\delta_{I2,0}) \\ -sin(\delta_{I2,0}) & cos(\delta_{I2,0}) \end{bmatrix} \Delta\bar{v}_{2,I2}^{dq} + \begin{bmatrix} -\bar{v}_{2,I2,0}^{d} sin(\delta_{I2,0}) + \bar{v}_{2,I2,0}^{q} cos(\delta_{I2,0}) \\ -\bar{v}_{2,I2,0}^{d} cos(\delta_{I2,0}) - \bar{v}_{2,I2,0}^{q} sin(\delta_{I2,0}) \end{bmatrix} \Delta\delta_{I2} - \Delta\bar{v}_{2f,I2}^{dq} \right) \,, \tag{27}$$

and

$$\frac{d\Delta\bar{U}_{i,I2}^{dq}}{dt} = Y_b k_{ii,I2}(\Delta\bar{i}_{1,I2}^{*dq} - \Delta\bar{i}_{1f,I2}^{dq}) \,. \tag{28}$$

2.2.2. Outer Loop Power Control

The GFL IBR outer loop controls regulated the output active and reactive power by synthesizing the inner loop current references through the use of PI controllers. The PI controller equations were as follows:

$$\Delta\bar{i}_{1,I2}^{*d} = \sqrt{3/2} V_b k_{pp,I2}(\Delta\bar{P}_{I2}^{*} - (\bar{i}_{2f,I2,0}^{dq})^T \Delta\bar{v}_{2f,I2}^{dq} - (\bar{v}_{2f,I2,0}^{dq})^T \Delta\bar{i}_{2f,I2}^{dq}) + \Delta\bar{U}_{p,I2} \,, \tag{29}$$

$$\frac{d\Delta\bar{U}_{p,I2}}{dt} = \sqrt{3/2} V_b k_{ip,I2}(\Delta\bar{P}_{I2}^{*} - (\bar{i}_{2f,I2,0}^{dq})^T \Delta\bar{v}_{2f,I2}^{dq} - (\bar{v}_{2f,I2,0}^{dq})^T \Delta\bar{i}_{2f,I2}^{dq}) \,, \tag{30}$$

$$\Delta\bar{i}_{1,I2}^{*q} = -\sqrt{3/2} V_b k_{pp,I2}(\Delta\bar{Q}_{I2}^{*} - (\bar{i}_{2f,I2,0}^{dq})^T G_{ROT} \Delta\bar{v}_{2f,I2}^{dq} - (\bar{v}_{2f,I2,0}^{dq})^T G_{ROT} \Delta\bar{i}_{2f,I2}^{dq}) - \Delta\bar{U}_{q,I2} \,, \tag{31}$$

$$\frac{d\Delta\bar{U}_{q,I2}}{dt} = \sqrt{3/2}V_b k_{ip,I2}(\Delta\bar{Q}^*_{I2} - (\bar{I}^{dq}_{2f,I2,0})^T G_{ROT}\Delta\bar{v}^{dq}_{2f,I2} + (\bar{V}^{dq}_{2f,I2,0})^T G_{ROT}\Delta\bar{i}^{dq}_{2f,I2}) \,, \quad (32)$$

and

$$\frac{d\Delta\bar{i}^{dq}_{2f,I2}}{dt} = \omega_{c2,I2}(\begin{bmatrix} cos(\delta_{I2,0}) & sin(\delta_{I2,0}) \\ -sin(\delta_{I2,0}) & cos(\delta_{I2,0}) \end{bmatrix}\Delta\bar{i}^{dq}_{2,I2} + \begin{bmatrix} -\bar{i}^{d}_{2,I2,0}sin(\delta_{I2,0}) + \bar{i}^{q}_{2,I2,0}cos(\delta_{I2,0}) \\ -\bar{i}^{d}_{2,I2,0}cos(\delta_{I2,0}) - \bar{i}^{q}_{2,I2,0}sin(\delta_{I2,0}) \end{bmatrix}\Delta\delta_{I2} - \Delta\bar{i}^{dq}_{2f,I2}) \,, \quad (33)$$

2.2.3. Phase-Locked Loop

The GFL IBR used a synchronous reference frame phase-locked loop (PLL) to maintain synchronism between the control system RRF and the system RRF. This allowed the *dq* components to be DC quantities at steady state.

$$\Delta\omega_{I2} = \sqrt{2/3}V_b k_{ppll,I2}(-\sin\delta_{I2,0}\Delta\bar{v}^{d}_{2,I2} + \cos\delta_{I2,0}\Delta\bar{v}^{q}_{2,I2} - (\bar{v}^{d}_{2,I2,0}\cos\delta_{I2,0} + \bar{v}^{q}_{2,I2,0}\sin\delta_{I2,0})\Delta\delta_{I2}) + \Delta U_{pll,I2} \,, \quad (34)$$

$$\frac{d\Delta U_{pll,I2}}{dt} = \sqrt{2/3}V_b k_{ipll,I2}(-\sin\delta_{I2,0}\Delta\bar{v}^{d}_{2,I2} + \cos\delta_{I2,0}\Delta\bar{v}^{q}_{2,I2} - (\bar{v}^{d}_{2,I2,0}\cos\delta_{I2,0} + \bar{v}^{q}_{2,I2,0}\sin\delta_{I2,0})\Delta\delta_{I2}) \quad (35)$$

and

$$\frac{d\Delta\delta_{I2}}{dt} = \Delta\omega_{I2} - \omega_b\Delta\bar{\omega}_{I1} \,. \quad (36)$$

2.3. Synchronous Generator Model

The six winding, RRF, flux linkage model of the SG was obtained from [30]. The *dq* components in the referenced SG model (denoted *dr* and *qr*) were aligned such that the *qr*-axis is aligned with the *as*-axis when ωt is zero and the *dr*-axis lags the *qr*-axis by 90 degrees. As a result, the equations relating the SG stator currents and voltages in the system RRF ($i^{dq}_{s,G1}$ and $v^{dq}_{s,G1}$, respectively) to these quantities in the SG RRF ($i^{dqr}_{s,G1}$ and $i^{dqr}_{s,G1}$) were

$$\Delta\bar{i}^{dq}_{s,G1} = \begin{bmatrix} cos(\delta_{G1,0}) & -sin(\delta_{G1,0}) \\ sin(\delta_{G1,0}) & cos(\delta_{G1,0}) \end{bmatrix}\begin{bmatrix} \Delta\bar{i}^{qr}_{s,G1} \\ (-\Delta\bar{i}^{dr}_{s,G1}) \end{bmatrix} + \begin{bmatrix} -\bar{i}^{qr}_{s,G1,0}sin(\delta_{G1,0}) - (-\bar{i}^{dr}_{s,G1,0})cos(\delta_{G1,0}) \\ \bar{i}^{qr}_{s,G1,0}cos(\delta_{G1,0}) + (-\bar{i}^{dr}_{s,G1,0})sin(\delta_{G1,0}) \end{bmatrix}\Delta\delta_{G1} \quad (37)$$

and

$$\begin{bmatrix} \Delta\bar{v}^{qr}_{s,G1} \\ (-\Delta\bar{v}^{dr}_{s,G1}) \end{bmatrix} = \begin{bmatrix} cos(\delta_{G1,0}) & sin(\delta_{G1,0}) \\ -sin(\delta_{G1,0}) & cos(\delta_{G1,0}) \end{bmatrix}\Delta\bar{v}^{dq}_{LD1} + \begin{bmatrix} -\bar{v}^{d}_{LD1,0}sin(\delta_{G1,0}) + \bar{v}^{q}_{LD1,0}cos(\delta_{G1,0}) \\ -\bar{v}^{d}_{LD1,0}cos(\delta_{G1,0}) - \bar{v}^{q}_{LD1,0}sin(\delta_{G1,0}) \end{bmatrix}\Delta\delta_{G1} \,. \quad (38)$$

Thus, (37) and (38) were used to integrate the SG electrical model equations with the remainder of the microgrid model. The rotational equations of motion were

$$2H_{G1}\frac{d\Delta\bar{\omega}_{G1}}{dt} = \bar{T}_{m,G1} - \bar{\lambda}^{dr}_{s,G1,0}\Delta\bar{i}^{qr}_{s,G1} - \bar{i}^{qr}_{s,G1,0}\Delta\bar{\lambda}^{dr}_{s,G1} + \bar{\lambda}^{qr}_{s,G1,0}\Delta\bar{i}^{dr}_{s,G1} + \bar{i}^{dr}_{s,G1,0}\Delta\bar{\lambda}^{qr}_{s,G1} - D_{G1}\Delta\bar{\omega}_{G1} \quad (39)$$

and

$$\frac{d\Delta\delta_{G1}}{dt} = \omega_b(\Delta\bar{\omega}_{G1} - \Delta\bar{\omega}_{I1}) \,. \quad (40)$$

Additionally, the equation for the field winding flux linkage derivative was modified so that a field winding voltage $\Delta\bar{v}^{dr}_{f,G1}$ of 1.0 pu will correlate to 1.0 pu stator voltage when the generator was unloaded. This equation was

$$\frac{1}{\omega_b}\frac{d\Delta\bar{\lambda}^{dr}_{f,G1}}{dt} = -\bar{R}_{fd,G1}\Delta\bar{i}^{dr}_{f,G1} + \frac{\bar{R}_{fd,G1}}{\bar{X}_{md,G1}}\Delta\bar{v}^{dr}_{f,G1}. \quad (41)$$

Field winding flux and engine/governor dynamics were known to have relatively large time constants compared to IBR control dynamics. For this reason, the small-signal model of the SG featured a constant mechanical torque and field voltage, which neglected the influence of the governor and excitation system. Here, it is noted that the base case

inertia constant of the SG model used in the analyses in this work is 0.736 s, which was obtained from the manufacturer data of a similarly rated SG encountered by the authors in other research projects.

2.4. Network

The load denoted as LD1 in Figure 1 was modeled as a constant resistance, which caused the load voltage to be given by the following equation:

$$\Delta\bar{v}_{LD1}^{dq} = \bar{R}_{LD1}(\Delta\bar{i}_{2,I1}^{dq} + \Delta\bar{i}_{2,I2}^{dq} + \Delta\bar{i}_{s,G1}^{dq}) \,. \tag{42}$$

The lines denoted as LN1 and LN2 (connecting the GFM and GFL IBR to the load in Figure 1, respectively) were modeled as series RL circuits. The line currents i_{LN1}^{dq} and i_{LN2}^{dq} were set equal to the respective IBR point of common coupling (PCC) currents i_{I1}^{dq} and i_{I2}^{dq}. Solving for the IBR PCC voltages in terms of the PCC current derivatives produced

$$\Delta\bar{v}_{3,I1}^{dq} = \frac{\bar{L}_{LN1}}{\omega_b}\frac{d\Delta\bar{i}_{2,I1}^{dq}}{dt} - (\bar{\omega}_0\bar{L}_{LN1}G_{ROT} - \bar{R}_{LN1})\Delta\bar{i}_{2,I1}^{dq} + \Delta\bar{v}_{LD1}^{dq} \tag{43}$$

and

$$\Delta\bar{v}_{3,I2}^{dq} = \frac{\bar{L}_{LN2}}{\omega_b}\frac{d\Delta\bar{i}_{2,I2}^{dq}}{dt} - (\bar{\omega}_0\bar{L}_{LN2}G_{ROT} - \bar{R}_{LN2})\Delta\bar{i}_{2,I2}^{dq} + \Delta\bar{v}_{LD1}^{dq} \,. \tag{44}$$

The line current variables were eliminated by substituting (43) into (5) and (44) into the differential equation, resulting in $\frac{d\Delta\bar{i}_{2,I2}^{dq}}{dt}$ (not shown, but readily obtained by replacing I1 variables with I2 variables in (5)). The remaining algebraic equations provided above were substituted into the differential equations and rearranged to obtain the complete, linear, state space model of the single GFM IBR microgrid illustrated in Figure 1.

3. EMT Model of a Multiple GFM IBR Microgrid

To determine if observations from the single GFM IBR microgrid analysis extended to a more complex system, an additional microgrid model featuring multiple GFM IBRs and SGs was developed. This was achieved via the modification of the Banshee Distribution System model, which was developed for the benchmarking of commercial microgrid control systems [31]. The loads were converted to constant impedance models. Existing DER models were replaced with the nonlinearized versions of the models presented in Sections 2.1 through 2.4. Additional GFM IBR and SG models were added to obtain the model shown in Figure 2. The Banshee Distribution System model network data were accessed from a publicly available GitHub repository [32]. The DER model parameters are placed in Table A2 of the Appendix A. The model was developed and simulated using the RTDS Technologies Novacor simulation platform due to the availability of the banshee model as an existing example in the RSCAD modeling package. This model was referred to as the Multiple GFM IBR Microgrid to differentiate it from the system shown in Figure 1.

In this case, prime mover and excitation system models were included in the SG generator subsystems to represent diesel internal combustion engine generating sets. The prime mover model was similar to other models found in the literature where the engine was modeled as a fixed delay and the fuel system actuator as a low-pass filter [27,33]. The prime mover model parameters were experimentally determined in order to produce the behavior representative of commercially available internal combustion engine generator sets according to the transient frequency response metrics found in ISO Std. 8528 [34]. A first-order Padé approximation was used to linearize the fixed time delay. The prime mover model block diagram is shown in Figure 3.

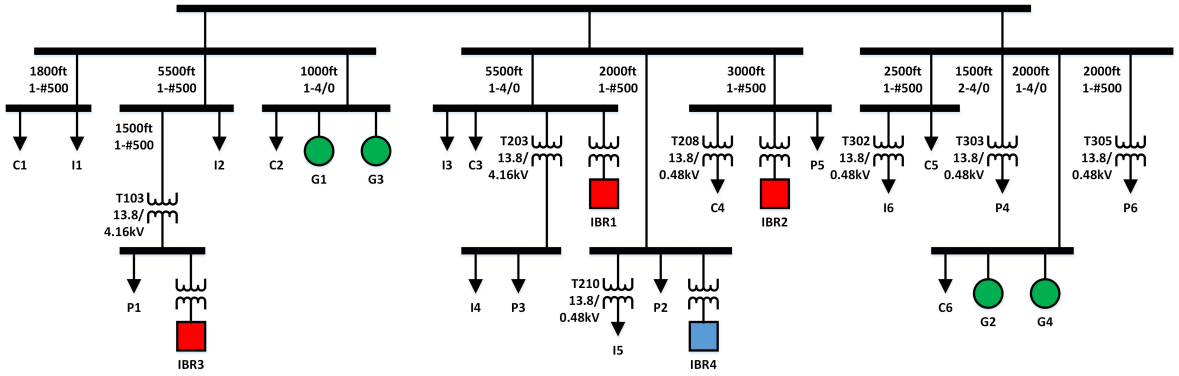

Figure 2. Single-line diagram of the Multiple GFM IBR Microgrid (synchronous generator = green circle, GFM IBR = red squares:, and GFL IBR = blue square).

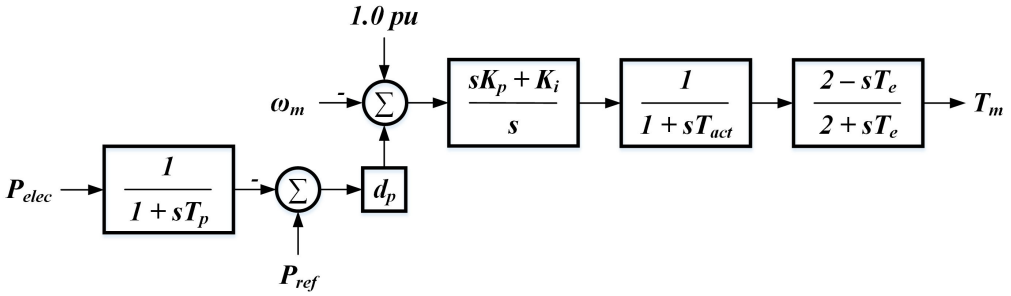

Figure 3. Block diagram of the governor and engine model used for electromagnetic transients (EMT) simulation of the microgrid shown in Figure 2.

The excitation system model was based on the IEEE-type AC5C model [35], which represented brushless excitation systems, and was linearized by neglecting the saturation of the rotating exciter. This model is provided in Figure 4.

The EMT model was used to simulate several generation trip scenarios with a time step of 50 µs. Results and analysis obtained from the simulation of this model will be discussed in Section 4.3.

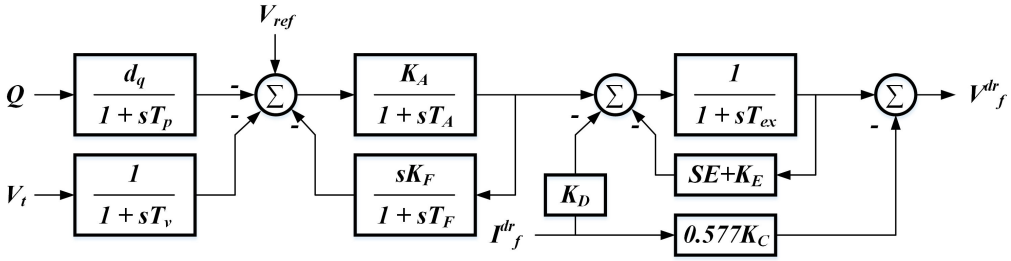

Figure 4. Block diagram of the excitation system model used for EMT simulation of the microgrid shown in Figure 2.

4. Results

4.1. Validation of the Small-Signal Model

This section provides a validation of the small-signal model presented in Section 2. Validation was performed by simulating both the small-signal and EMT models of the microgrid shown in Figure 1 and comparing the responses of select state variables. Two cases featuring different disturbances were tested. First, the state variables were recorded in the EMT model before and after the disturbance was applied. These values were used as the small-signal model states at the pre- and post-disturbance operating points ($\mathbf{x}(t_0)$ and $\mathbf{x}(\infty)$, respectively). The post-disturbance operating point was used to obtain the state

matrix **A**. Then, the small-signal model was simulated using Matlab/Simulink with the default fixed-step solver and 50 µs time step according to

$$\mathbf{x}(t) = \left\{ \begin{array}{ll} \int_{t_0}^{t} \mathbf{A}(\mathbf{x}(t) - \mathbf{x}(\infty)\, d\tau, & t > t_0 \\ \mathbf{x}(t_0), & t \leq t_0 \end{array} \right\}. \tag{45}$$

The first disturbance was a reduction in the load LD1 shunt resistance, which caused a 0.2 pu (on the system base) increase in the active power consumed by load. The relevant setpoints and parameters used for this simulation are summarized in Table 2.

Table 2. Load acceptance EMT simulation setpoints and parameters. System base: 60 Hz, 2.5 MVA, 4160 V.

Setpoint/Parameter	Value (pu)	Setpoint/Parameter	Value (pu)
$\bar{\omega}^*_{I1}$	1.0	$\bar{T}_{m,G1}$	0.4928
$\bar{P}^*_{I1}$	−0.0305	$\bar{v}^{dr}_{f,G1}$	1.32
$\bar{v}^*_{I1}$	1.026	$\bar{R}_{LD1}(t \leq t_0)$	1.0
$\bar{P}^*_{I2}$	0.4017	$\bar{R}_{LD1}(t > t_0)$	0.833
$\bar{Q}^*_{I2}$	0.0241		

The responses of the selected state variables from the EMT simulation and small-signal model simulation are compared in Figure 5.

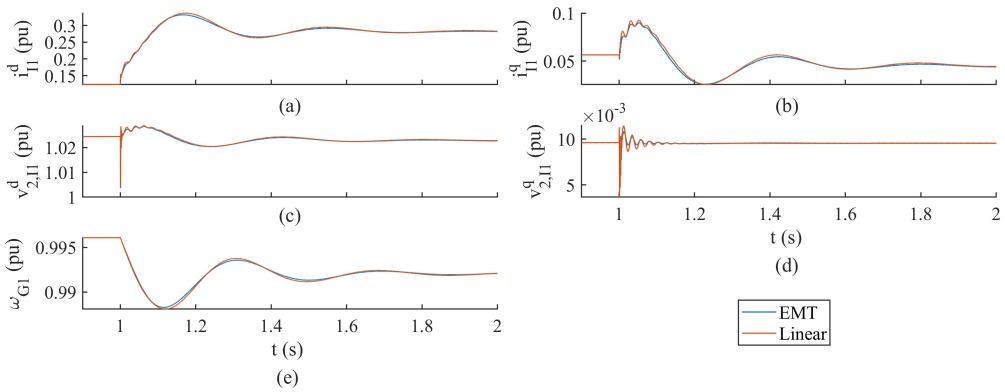

Figure 5. Comparison of model states in response to load acceptance for EMT and small-signal models of the single GFM IBR microgrid. The EMT states are in blue and small-signal model states are in red; (**a**,**b**) show the GFM IBR output currents; (**c**,**d**) show the GFM IBR filter capacitor voltages; and (**e**) shows the generator rotor speed.

Higher resolution plots of the GFM IBR filter capacitor voltages are provided in Figure 6 to illustrate the model agreement for higher-frequency modes.

A contingency where the GFL IBR was tripped offline was simulated for the second case. The relevant setpoints and parameters used for this simulation are summarized in Table 3.

The responses of the selected state variables for the GFL IBR contingency case are compared in Figure 7 with higher-resolution plots of the filter voltages in Figure 8.

Table 3. GFL IBR Contingency EMT Simulation Setpoints and Parameters. System Base: 60 Hz, 2.5 MVA, 4160 V.

Setpoint/Parameter	Value (pu)	Setpoint/Parameter	Value (pu)
$\bar{\omega}^*_{I1}$	1.0	$\bar{T}_{m,G1}$	0.6
$\bar{P}^*_{I1}$	0.0	$\bar{v}^{dr}_{f,G1}$	1.483
$\bar{v}^*_{I1}$	1.0	$\bar{R}_{LD1}(t \leq t_0)$	0.8
$\bar{P}^*_{I2}$	0.1	$\bar{R}_{LD1}(t > t_0)$	0.8
$\bar{Q}^*_{I2}$	0.0		

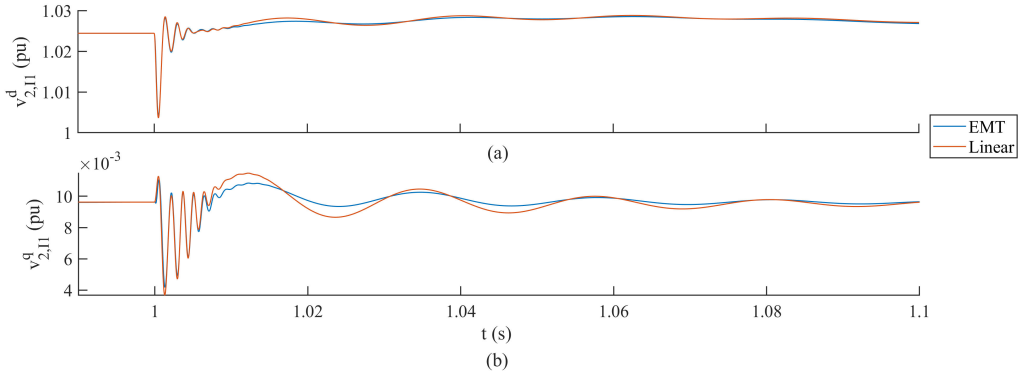

Figure 6. Higher resolution comparison of the GFM IBR filter capacitor voltages in response to load acceptance for EMT and small-signal models of the single GFM IBR microgrid. The EMT states are in blue and small-signal model states are in red; (**a**) shows the *d*-axis voltage and (**b**) shows the *q*-axis voltage.

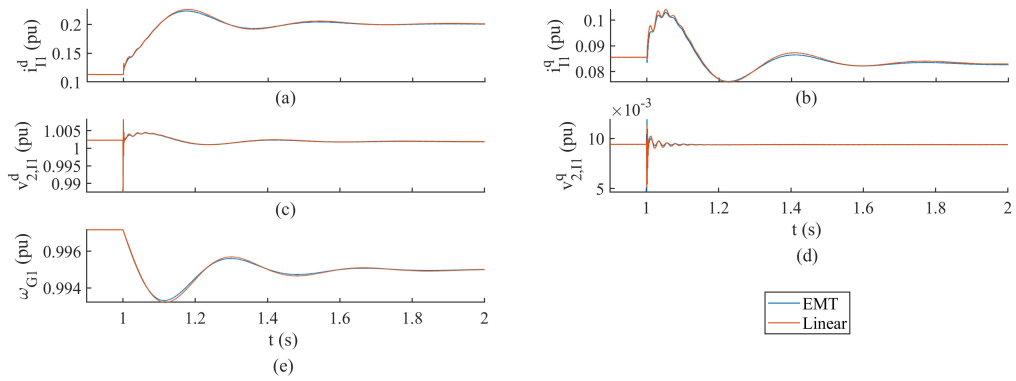

Figure 7. Comparison of model states in response to GFL IBR contingency for EMT and small-signal models of the single GFM IBR microgrid. The EMT states are in blue and small-signal model states are in red; (**a**,**b**) show the GFM IBR output currents; (**c**,**d**) show the GFM IBR filter capacitor voltages; and (**e**) shows the generator rotor speed.

Note that the small-signal model cannot reproduce the behavior of an EMT breaker model, which includes an RC-snubber circuit as well as single-phase switching at the current waveform zero crossings. Therefore, the GFL IBR model was replaced with controlled current sources, which injected the pre-disturbance GFL IBR point of common coupling currents. To simulate the contingency, the current source references were instantaneously set to zero. Additionally, to reflect the GFL IBR contingency in the small-signal model, the equations and variables related to the GFL IBR dynamics were removed before forming the state matrix.

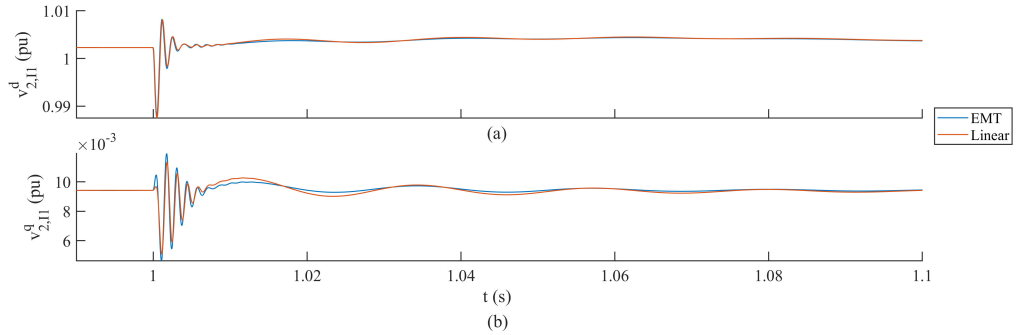

Figure 8. Higher resolution comparison of the GFM IBR filter capacitor voltages in response to GFL IBR contingency for EMT and small-signal models of the single GFM IBR microgrid. The EMT states are in blue and small-signal model states are in red; (**a**) shows the *d*-axis voltage and (**b**) shows the *q*-axis voltage.

The EMT and small-signal model state variable responses in Figure 5 through to Figure 8 exhibit similar amplitudes and frequencies. The two test cases resulted in similar behavior, which was expected since load acceptance and generation loss both cause rapid increases in load for the grid-forming inverter and synchronous generator. The authors selected these types of disturbances as they are highly applicable to the transient load sharing problem.

4.2. Modal Analysis of Small-Signal Microgrid Model

A state matrix was formed by using the small-signal model discussed in Section 2 and post-load acceptance operating point discussed in Section 4.1. This matrix was used as the basis to conduct a sensitivity analysis of the eigenvalues and eigenvectors to variation in the GFM IBR P-F droop parameter $d_{p,I1}$ and the synchronous generator inertia H_{G1}. The analysis began by identifying modes with low-to-moderate damping ratios ζ that were both sensitive to $d_{p,I1}$ and participated in the state variable $i^d_{1,I1}$. The variable $i^d_{1,I1}$ was selected because the choice of RRF orientation caused the disturbances associated with fluctuation in the GFM IBR output active power to appear predominantly as an increase in the GFM IBR ouput current *d*-axis component magnitude. This can be seen from Figure 5. Thus, the presence of modes with low ζ and significant participation in $i^d_{1,I1}$ were indicative of a poorly damped GFM IBR output current response to an active power-related disturbance (such as generation trip or load acceptance) and an elevated risk of tripping overcurrent protections. The eigenvalues of the state matrix were iteratively computed using the eig() function of the Numpy linalg module in Python for a set of $d_{p,I1}$ values ranging from 0.002 pu/pu to 0.2 pu/pu on the GFM IBR base, and the eigenvalue trajectories are displayed in Figure 9.

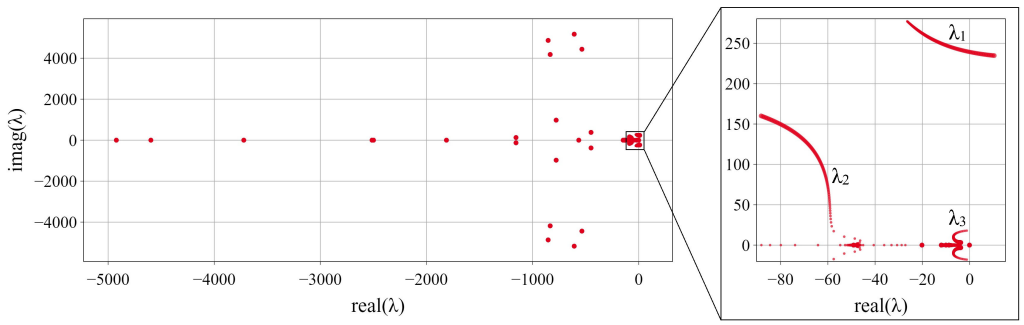

Figure 9. Sensitivities of the single GFM IBR microgrid system (see Figure 1) eigenvalues to $d_{p,I1}$. Increasing marker size indicates increase in $d_{p,I1}$ from 0.002 pu/pu to 0.2 pu/pu on GFM IBR base. The inset shows underdamped eigenvalues that were found to be sensitive to $d_{p,I1}$, which have been labeled λ_1, λ_2, and λ_3.

Figure 9 shows three underdamped modes (see inset at right), which responded significantly to the variation in the grid-forming inverter P-F droop $d_{p,I1}$. These were designated in order of decreasing damped natural frequency ω_d as the fast λ_1, medium λ_2, and slow λ_3 modes. The main trends observed were that both λ_1 and λ_3 exhibited very low damping ratios initially. Then, λ_3 experienced a significant damping improvement, while λ_1 moved toward the right hand side (RHS) of the real axis, eventually leading to instability and imposing a limit on any damping improvement to λ_3. λ_2 exhibited a worst-case damping ratio ζ of 0.45, which corresponded to an overshoot of about 20% for a second-order system and therefore was not considered a problem mode. In the remaining analysis, a 20% maximum overshoot was used as the threshold to determine if a response was well damped. This threshold was chosen as it had been encountered in overcurrent and overload protection functions of commercially available control systems for both IBRs and SGs in the authors experience.

In the next step, the inertia constant of the SG H_{G1} varied from 0.368 s to 3.312 s. The objective was to determine how the mode trends respond to the changes in the system inertia. This was deemed an important consideration as there was consensus from the power systems research community that the integration of renewables would lead to lower-inertia power systems [4,5,12,21,22]. At a more local level, islanded microgrids may feature groups of smaller SGs [1] that perform load-dependent start/stop operations to ensure that individual units operate at minimum loads, thus causing the amount of physical inertia to vary depending on the microgrid load and renewables' profiles. For this reason, a simultaneous sensitivity of the modes λ_1–λ_3 to the GFM IBR P-F droop $d_{p,I1}$ and H_{G1} is presented in Figure 10.

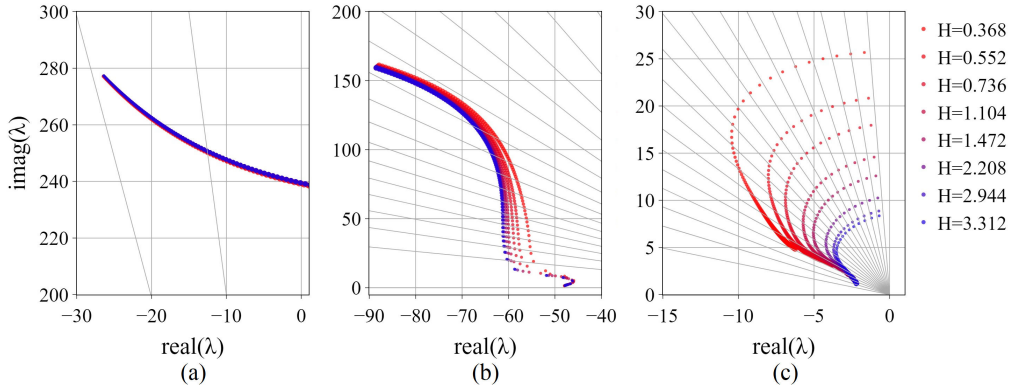

Figure 10. Sensitivities of λ_1, λ_2, and λ_3 to $d_{p,I1}$ for variation in H_{G1}. Increasing marker size indicates increase in $d_{p,I1}$ from 0.002 pu/pu to 0.2 pu/pu on GFM IBR base. Gray radial lines indicate constant damping ratio. (**a**) Sensitivity of λ_1. (**b**) Sensitivity of λ_2. (**c**) Sensitivity of λ_3.

The main observation from Figure 10 was that sensitivity trends of the fast mode λ_1 and medium mode λ_2 to the GFM IBR P-F droop $d_{p,I1}$ were little affected by the SG inertia constant H_{G1} value. The trends for the slow mode λ_3 showed that the natural frequency ω_n was reduced by increasing H_{G1}; however, the trends in damping were very similar as indicated by the constant damping ratio ζ lines in subplot (c). Therefore, it was predicted that the damping improvement in the GFM IBR output current magnitude determined through detailed simulation would exhibit only minor sensitivity to H_{G1}. At this point, further modal analysis was performed for only λ_1 and λ_3 due to finding that λ_2 exhibited suitable damping ratios regardless of the values of $d_{p,I1}$ or H_{G1} tested.

The participation factors are often used in modal analysis to determine how the system modes contribute to the response of the system states when perturbed away from the operating point to some initial condition, denoted as $\mathbf{x}(0)$. This is readily observed by

the time domain solution of the linear system response $\mathbf{x}(t)$ (assuming the system inputs are constant):

$$\mathbf{x(t)} = \mathbf{U}\begin{bmatrix} e^{\lambda_1 t} & & 0 \\ & e^{\lambda_2 t} & \\ 0 & & e^{\lambda_n t} \end{bmatrix}\mathbf{V}\mathbf{x}(\mathbf{0}) = \mathbf{U}e^{\mathbf{\Lambda} t}\mathbf{V}\mathbf{x}(\mathbf{0}) \tag{46}$$

where the columns of **U** are the right eigenvectors (also known as mode shapes) and the columns of **V** are the left eigenvectors. Thus, the term containing the k^{th} mode λ_k and the initial value of the i^{th} state $x_i(0)$ in the solution of the i^{th} state $x_i(t)$ is

$$U(i,k)e^{\lambda_k t}V^T(i,k)x_i(0) \tag{47}$$

and $U(i,k)V^T(i,k)$ is the participation factor. $P(i^d_{1,I1},\lambda_1)$ and $P(i^d_{1,I1},\lambda_3)$ were used to denote the participation of the fast mode λ_1 and the slow mode λ_3 in the GFM IBR d-axis current $i^d_{1,I1}$, respectively. The sensitivities of $P(i^d_{1,I1},\lambda_1)$ and $P(i^d_{1,I1},\lambda_3)$ to the GFM IBR P-F droop $d_{p,I1}$ and SG inertia constant H_{G1} are given in Figure 11.

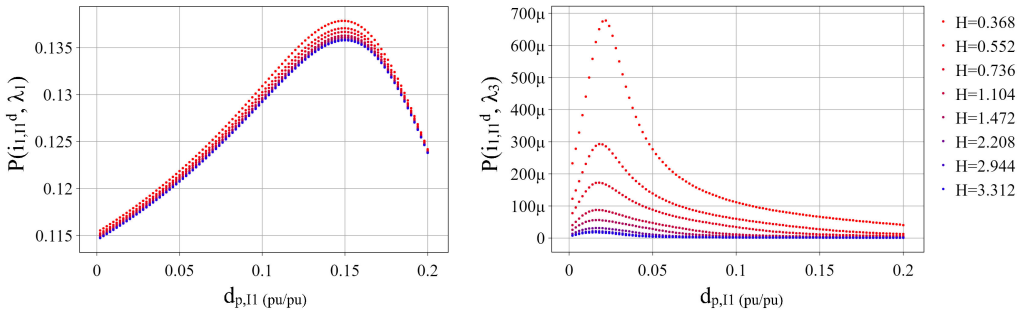

(**a**) (**b**)

Figure 11. Sensitivities of (**a**) $P(i^d_{1,I1},\lambda_1)$ and (**b**) $P(i^d_{1,I1},\lambda_3)$ to $d_{p,I1}$ and H_{G1}.

The participation factor trends suggested that the fastest mode λ_1 would be the dominate oscillatory mode observed in the response of the GFM IBR d-axis current $i^d_{1,I1}$ regardless of the value of the GFM IBR P-F droop $d_{p,I1}$ and SG inertia constant H_{G1}. In contrast, λ_3 would likely not be observed at all. It was noted that there are other underdamped oscillatory modes that were not studied due to insensitivity to both $d_{p,I1}$ and H_{G1}. However, in referring once again to Figure 9, these modes had ω_n greater than 4000 rad/s and a damping ratio ζ of at least 0.1 and so were likely to settle before contributing to an overcurrent condition.

The implications of the analysis thus far was that the smallest value of the GFM IBR P-F droop $d_{p,I1}$ would yield the best damping of the GFM IBR output current magnitude response to a load or generation disturbance. This prediction was tested with 198 simulations of the EMT model of the single GFM IBR microgrid performed for 22 different values of $d_{p,I1}$ and nine values of the SG inertia constant H_{G1}. The output current magnitude of the GFM IBR was recorded for each combination of parameters in response to a 0.2 pu load increase occuring at $t = 20$ s. The EMT simulation was carried out using built-in stationary reference frame models of passive and active components available in the Matlab/Simulink Specialized Power System toolbox. As a result, the magnitude was obtained by first applying (7) (ωt can be arbitrary) to the three-phase currents and then calculating the magnitude as

$$|i_{1,I1}| = \sqrt{(i^d_{1,I1})^2 + (i^q_{1,I1})^2}. \tag{48}$$

A subset of the results are shown in Figures 12 and 13.

The most notable observation from these figures was the prevalence of the slow mode λ_3 in response to the GFM IBR output current magnitude $|i_{1,I1}|$ when the GFM IBR P-F droop $d_{p,I1}$ was less than 0.05 pu/pu (on the GFM IBR's base). This seemed to contradict the

indication of mode participations by the participation factors shown in Figure 11. This result was significant given that participation factors were traditionally used to identify dominant modes associated with specific state variables in power systems (see [26,36]). Additionally, the use of these metrics continued to be found in more recent works, addressing power system frequency stability improvement [37,38]).

It was apparent that the substantial participation of the slow mode λ_3 in the GFM IBR current magnitude $|i_{1,I1}|$ observed in the subplots of Figures 12 and 13 may be due to the excitation of λ_3 by the initial conditions of states other than the GFM IBR d-axis current $i^d_{1,I1}$. This would not be reflected by the values of the participation factor $P(i^d_{1,I1}, \lambda_3)$ illustrated in Figure 11. To determine if another state was exciting λ_3, the elements of the matrix containing the left eigenvectors of the model state matrix $\mathbf{A}$ (henceforth referred to as the mode excitations) correlating to the fast mode λ_1 and slow mode λ_3 for the case when $d_{p,I1}$ = 0.01 pu/pu and H_{G1} = 0.736 s are tabulated in Table 4.

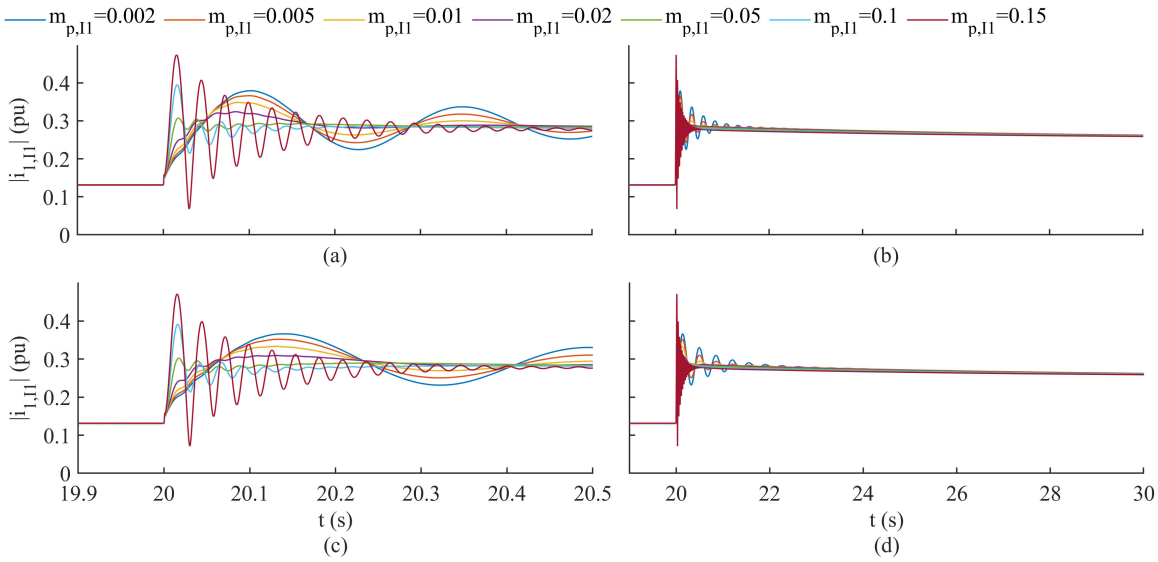

Figure 12. EMT simulations of 0.2 pu load acceptance in single GFM IBR microgrid (see Figure 1) for variations in $d_{p,I1}$ and H_{G1}. Plots illustrate response of GFM IBR output current magnitude $|i_{1,I1}|$ to load disturbance. (**a**) Short time and (**b**) full transient response when H_{G1} is 0.368 s. (**c**) Short time and (**d**) full transient response when H_{G1} is 0.736 s.

From Table 4, the excitation of the slow mode λ_3 by the SG rotor speed ω_{G1} was found to be several orders of magnitude larger than the excitation of λ_3 by the GFM IBR d-axis current $i^d_{1,I1}$. This explained the discrepancy between the values of the participation factor $P(i^d_{1,I1}, \lambda_3)$ from Figure 11 and the EMT simulation results in Figures 12 and 13. It was proposed to use a new metric to estimate the participation of a mode λ_k in a state x_i, which would be denoted $Q(x_i, \lambda_k)$ and given by

$$Q(x_i, \lambda_k) = U(i,k) \sum_{j=1}^{n} V(k,j) \tag{49}$$

The sensitivities of $Q(i^d_{1,I1}, \lambda_1)$ and $Q(i^d_{1,I1}, \lambda_3)$ to $d_{p,I1}$ and H_{G1} are plotted in Figure 14.

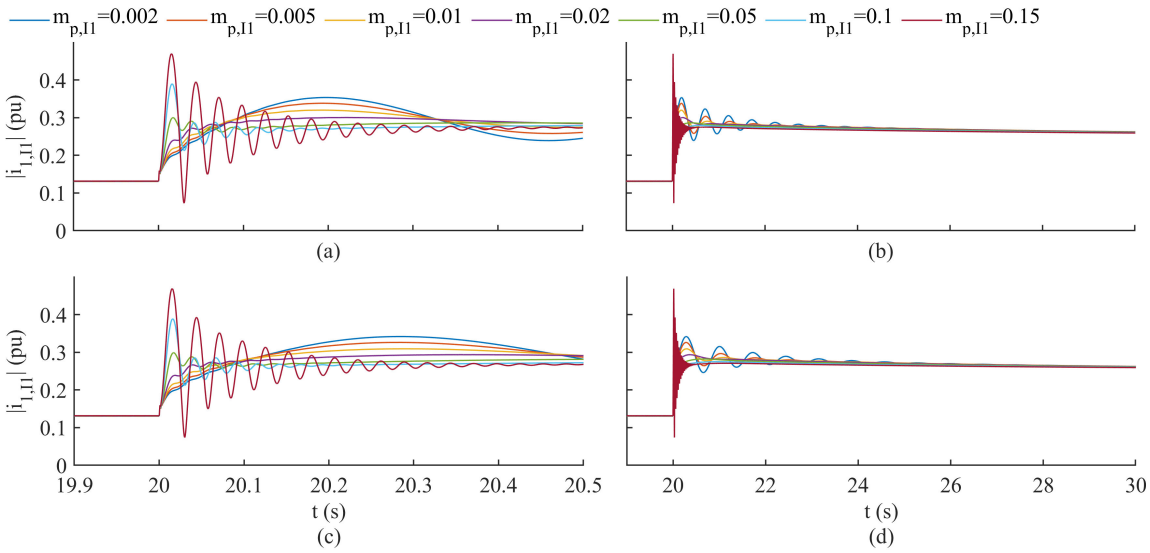

Figure 13. EMT simulations of 0.2 pu load acceptance in single GFM IBR microgrid (see Figure 1) for variations in $d_{p,I1}$ and H_{G1}. Plots illustrate response of GFM IBR output current magnitude $|i_{1,I1}|$ to load disturbance. (**a**) Short time and (**b**) full transient response when H_{G1} is 1.472 s. (**c**) Short time and (**d**) full transient response when H_{G1} is 2.944 s.

Table 4. λ_1 and λ_3 excitations by states when $d_{p,I1}$ is 0.01 pu/pu and H_{G1} is 0.736 s for single GFM IBR microgrid.

State	λ_1	λ_3	State	λ_1	λ_3	State	λ_1	λ_3	State	λ_1	λ_3
$i^d_{2,I1}$	2.781	0.057	$v^q_{2,I2}$	0.007	0.002	$v^d_{2f,I1}$	0.873	0.016	$i^q_{1f,I2}$	0.033	0.010
$i^q_{2,I1}$	2.860	0.128	δ_{G1}	5.955	4.545	$v^q_{2f,I1}$	0.881	0.034	$v^d_{2f,I2}$	0.051	0.076
$i^d_{1,I1}$	1.188	0.002	$\lambda^{dr}_{s,G1}$	4.579	0.065	$i^d_{2f,I1}$	0.796	0.020	$i^d_{2f,I2}$	0.001	0.005
$i^q_{1,I1}$	1.206	0.003	ω_{G1}	2.233	101.717	$i^q_{2f,I1}$	0.841	0.007	$v^q_{2f,I2}$	0.091	0.024
$i^d_{2,I2}$	0.007	0.002	$\lambda^{qr}_{s,G1}$	4.474	0.254	$P_{f,I1}$	0.197	0.440	$i^q_{2f,I2}$	0.001	0.002
$i^q_{2,I2}$	0.014	0.004	$\lambda^{dr}_{k,G1}$	0.416	1.426	$Q_{f,I1}$	0.840	0.057	δ_{I2}	0.010	0.000
$i^d_{1,I2}$	0.064	0.072	$\lambda^{dr}_{f,G1}$	1.046	6.097	$U^d_{i,I1}$	13.178	0.310	$U^d_{i,I2}$	0.124	2.593
$i^q_{1,I2}$	0.090	0.025	$\lambda^{qr}_{k1,G1}$	0.546	0.836	$U^q_{i,I1}$	13.372	0.532	$U^q_{i,I2}$	0.211	0.912
$v^d_{2,I1}$	0.340	0.001	$\lambda^{qr}_{k2,G1}$	1.199	0.689	$U^d_{v,I1}$	7.145	0.483	$U_{p,I2}$	0.134	2.910
$v^q_{2,I1}$	0.345	0.002	$i^d_{1f,I1}$	0.787	0.003	$U^q_{v_I1}$	7.251	0.829	$U_{q,I2}$	0.229	1.024
$v^d_{2,I2}$	0.005	0.006	$i^q_{1f,I1}$	0.790	0.006	$i^d_{1f,I2}$	0.006	0.017	$U_{pll,I2}$	0.000	0.000

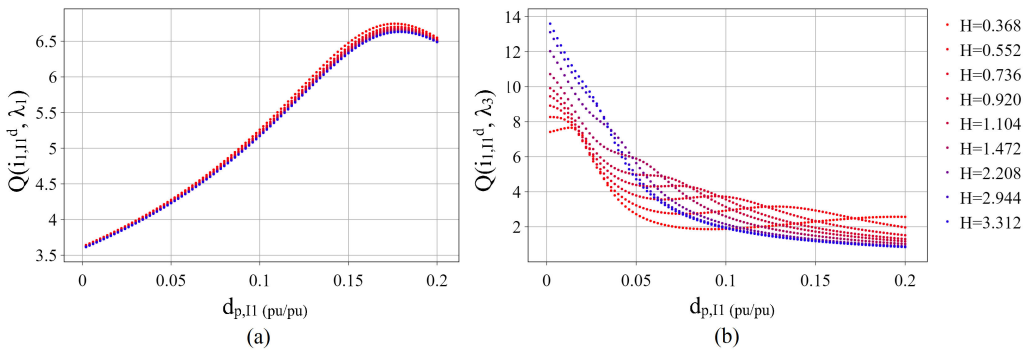

Figure 14. Sensitivity of (**a**) $Q(i^d_{1,I1}, \lambda_1)$ and (**b**) $Q(i^d_{1,I1}, \lambda_3)$ to $d_{p,I1}$ (pu/pu values are on GFM IBR base) and H_{G1}.

The following observations arose from a comparison of Figures 11–14:

- In contrast to the participation factors, the $Q(x_i, \lambda_k)$ metrics clearly indicated the contribution of λ_3 in response to $|i_{1,I1}|$;
- The $Q(x_i, \lambda_k)$ metrics predicted the inversion of the relative dominance of the slow mode λ_3 and fast mode λ_1 in response to the GFM IBR current magnitude $|i_{1,I1}|$ as the GFM IBR P-F droop $d_{p,I1}$ increased toward the stability limit;
- $Q(i^d_{1,I1}, \lambda_1)$ exhibited almost no sensitivity to the SG inertia constant H_{G1} while $Q(i^d_{1,I1}, \lambda_3)$ showed some sensitivity to H_{G1} but the general trend was the same.

The smallest overshoot MP_{min} occurring for each H_{G1} value and the corresponding value of P-F droop parameter $d_{p,I1,min}$ are tabulated in Table 5.

Table 5 shows that the optimal value of $d_{p,I1}$ exhibited little sensitivity to H_{G1} as $d_{p,I1,min}$ decreased by 0.01 pu/pu. The total improvement to MP_{min} was 16.8%. Additionally, the values of MP_{min} showed diminishing returns as H_{G1} increased. These results suggested that re-tuning the value of $d_{p,I1}$ when the physical inertia in the system changed would confer minimal benefit since even the best case scenario resulted in greater than 20% maximum overshoot.

Table 5. Smallest overshoot MP_{min} of $|i_{1,I1}|$ and the corresponding value of $d_{p,I1}$ for each EMT simulation of the single GFM IBR microgrid.

$H_{G1}(s)$	$MP_{min}(\%)$	$d_{p,I1,min}$ (pu/pu)
0.368	40.9	0.045
0.552	34.6	0.035
0.736	32.0	0.035
0.920	30.4	0.040
1.104	29.0	0.040
1.472	27.2	0.040
2.208	25.4	0.040
2.944	24.4	0.040
3.312	24.1	0.035

4.3. EMT Simulation of the Multiple GFM IBR Microgrid

EMT simulations of the microgrid shown in Figure 2 were performed to determine if the same trends obtained from analyzing the single GFM IBR microgrid (Figure 1) would be observed. Details about the simulation platform and settings are given in Section 3. Four case studies were developed such that the number of diesel generators in operation varied from one to four. In each case study, the GFL IBR was tripped offline, resulting in a substantial load acceptance for the remaining DER. The cases were designed to result in approximately the same pre- and post-disturbance loading of the GFM IBRs (0.55 pu and 0.9 pu, respectively) and the diesel generators (0.48 pu and 0.8 pu, respectively). This was accomplished by adjusting the pre-disturbance GFL IBR active and reactive power setpoints and connecting only a subset of the constant impedance loads. These scenarios are described in Table 6.

Table 6. Multiple GFM IBR microgrid cases.

Case	SG	IBR4 P,Q	Loads	Total Load P,Q
1	G2	2.0 MW, 1.0 MVAR	C2–C5, P4	4.74 MW, 1.57 MVAR
2	G1, G2	2.8 MW, 0.1 MVAR	C1–C6, P5	5.63 MW, 1.70 MVAR
3	G1–G3	3.6 MW, 1.5 MVAR	C1–C6, I5, P1, P6	7.16 MW, 2.44 MVAR
4	G1–G4	4.0 MW, 2.0 MVAR	C1–C6, I2, P1–P3, P6	8.94 MW, 4.04 MVAR

For each case, several simulations were run in which the value of the P-F droop parameter shared by all three GFM IBRs $d_{p,GFM}$ varied from 0.02 pu/pu to 0.10 pu/pu (on the GFM IBR base) to determine the effect, if any, on the magnitude of the output current of the GFM IBRs (calculated according to (48)). The starting value of $d_{p,GFM}$ resulted in

the maximum output of the GFM IBRs occurring for a frequency of 58.8 Hz at steady state, which was the continuous operation lower limit for distributed IBRs per the IEEE Std. 1547-2018 frequency ride-through requirements [39]. Additionally, it should be noted that the GFM IBR models were identical in structure and parameters and their output current response to the generation trip was found to be nearly the same across all cases and values of $d_{p,GFM}$ tested, as illustrated by the traces in Figure 15.

This was expected due to the similarity of these models and the fact that the network impedances are smaller than the GFM IBR LCL filter impedances. As a result, further figures containing simulation results will only show the response of IBR1 output current magnitude $i_{1,IBR1}$ for space considerations.

A subset of the results of the Case 1 through Case 4 simulations are shown in Figures 16 and 17. From examining the output current responses for the Multiple GFM IBR Microgrid simulations, it was observed that the response contains both fast (hundreds of rad/s) and slow (tens of rad/s) components that were easily distinguished due to their disparities in time scales.

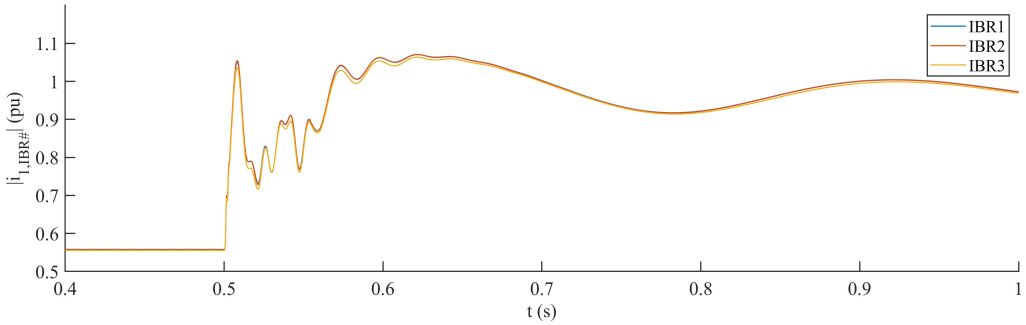

Figure 15. Case 1 IBR1–IBR3 output current responses to generation trip when $d_{p,GFM}$ is 0.02 pu/pu on the GFM IBR base.

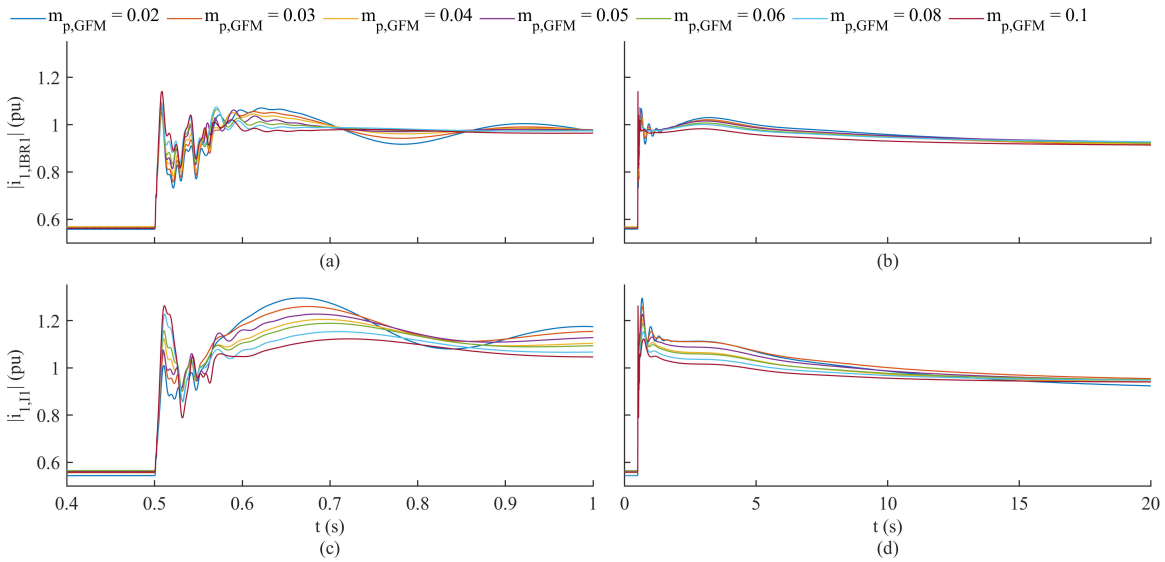

Figure 16. EMT simulations of IBR4 trip in Multiple GFM IBR Microgrid (see Figure 2) for variations in $d_{p,GFM}$ and the number of SGs (as indicated by the case number in Table 6). Plots illustrate response of IBR1 output current magnitude $|i_{1,IBR1}|$ to generation disturbance. (**a**) Short time and (**b**) full transient response for Case 1 (one SG). (**c**) Short time and (**d**) full transient response for Case 2 (two SGs).

This was similar to the distribution of modes observed in Figures 12 and 13. For comparison with the EMT simulation results of the single GFM IBR microgrid, the same data pertaining to the smallest overshoots MP_{min} of $|i_{1,IBR1}|$ are record in Table 7.

Table 7. Smallest overshoot MP_{min} of $|i_{1,IBR1}|$ and corresponding $d_{p,GFM}$ values from EMT simulations of the Multiple GFM IBR Microgrid.

Case	MP_{min} (%)	$d_{p,GFM,min}$ (pu/pu)
1	44.9	0.05
2	63.9	0.06
3	67.4	0.08
4	63.9	0.09

From Figures 16 and 17, and Table 7, it was apparent that the introduction of the governor and exciter dynamics significantly affected the settling time of the IBR1 output current magnitude $|i_{1,IBR1}|$ and decreased the damping of the slower modes. Table 7 shows a substantial reduction in the effectiveness of tuning the GFM IBR P-F droop $d_{p,GFM}$ to improve the damping of the GFM IBR output current in the Multiple GFM IBR Microgrid as compared to the single GFM IBR microgrid. Interestingly, Table 7 shows that the greatest damping improvement to $|i_{1,IBR1}|$ occurred for the fewest number of SG cases and that the optimal value of $d_{p,GFM}$ exhibited significant sensitivity to the number of SGs in operation. These results revealed the importance of the detailed modeling of the governor and excitation systems despite large time constants associated with these subsystems. Overall, the damping improvement by tuning $d_{p,GFM}$ was still limited to an unsatisfactory level and the change in the smallest overshoot MP_{min} due to the variation in the number of SGs in operation was 19%. This was a similar result to the limited improvement in the damping and low sensitivity of MP_{min} to the SG inertia constant in the single GFM IBR microgrid analysis.

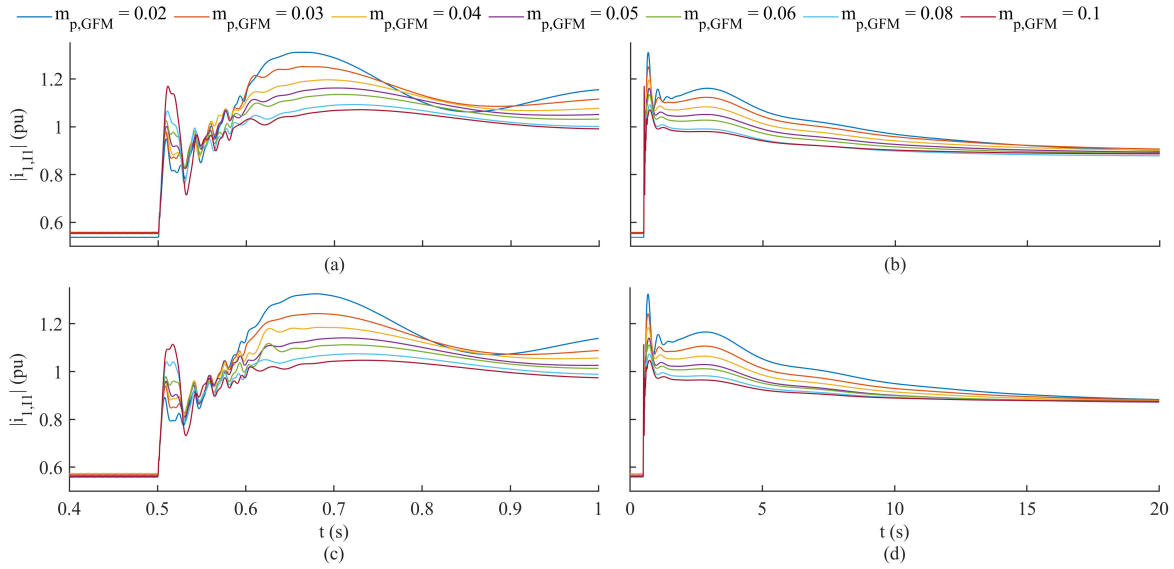

Figure 17. EMT simulations of IBR4 trip in Multiple GFM IBR Microgrid (see Figure 2) for variations in $d_{p,GFM}$ and number of SGs (as indicated by the case number in Table 6). Plots illustrate response of IBR1 output current magnitude $|i_{1,IBR1}|$ to generation disturbance. (**a**) Short time and (**b**) full transient response for Case 3 (three SGs). (**c**) Short time and (**d**) full transient response for Case 4 (four SGs).

5. Discussion

In this paper, the detailed modeling of a mixed-source microgrid containing a GFM IBR, GFL IBR, and SG was performed to create a simple yet effective platform for studying the phenomenon of transient load sharing between GFM-controlled IBRs and SGs (see Figure 1 in Section 2). The model was linearized to obtain the small signal equivalent in Sections 2.1–2.4. The linear model was analyzed in Section 4.2 to identify two important modes of interest contributing to the underdamped response of the GFM IBR output current to a load disturbance. This was compared to EMT simulations of the microgrid model in Figure 1. Notably, participation factors traditionally used to identify dominant modes associated with specific state variables in power systems did not predict the prevalence of the lower-frequency mode in the GFM IBR output current response. Alternatively, a metric was proposed, which better indicated the participations of each mode and the sensitivities of these participations to both the P-F droop parameter and SG inertia. Finally, EMT simulations were performed on a more complex microgrid (see Figure 2 in Section 3) and the results were compared with the modal analysis results. These led to three important findings relating to the influence of the P-F droop parameter on the GFM IBR output current damping:

1. The peak value of the GFM IBR output current in response to a load acceptance displayed high sensitivity to the P-F droop parameter.
2. The optimal value of P-F droop parameter in the Multiple GFM IBR Microgrid was dependent on the number of SGs in the system, with substantial variation in the optimal value and the lowest overshoot occurring with only one SG in the system (the greatest penetration of the GFM IBRs).
3. In the Multiple GFM IBR Microgrid, the lowest overshoot achieved was 44.9%.

The first finding was noteworthy as it was in direct contrast to prior work investigating interactions of GFM IBR and SG in [25]. The second finding was somewhat aligned with the results in [12,21,22], which established improvement in the damping of frequency transients in power systems as the ratio of GFM IBRs to SGs increases. Having found the GFM IBR output current to be highly coupled to the SG rotor speed through the slow mode λ_3, it could be concluded that the damping improvement extends to the GFM IBR output currents as well. However, the reduced-order modeling in these works failed to capture the higher-frequency modes, which would clearly contribute to the overcurrent tripping of the GFM IBRs. In the context of islanded microgrids with fewer resources, it was unclear whether the frequency stability improvement would offset an increased risk of cascading generation trips due to the greater proportions of devices with higher sensitivity to overcurrents. Finally, the main implication of the findings was that tuning the P-F droop parameter was not an effective approach to reducing the potential for overcurrent conditions for GFM IBR in response to large load and generation disturbances. This was consistently the result across simulations of both microgrid models. Furthermore, the value of P-F droop parameter that optimizes the current damping objective was sensitive to the number of SGs in operation, which would increase the computational burden of the P-F droop tuning approach for minimal payback. Future work on the transient load sharing of GFM IBRs and SGs will focus on developing auxiliary control loops that can enforce output power and current limits of the GFM IBR through the initial phase of the load or generation disturbance response, while still supporting load sharing objectives during the recovery and post-recovery phases.

Author Contributions: Conceptualization, J.W.; Funding acquisition, R.H.; Investigation, J.W.; Methodology, J.W.; Project administration, R.H.; Supervision, R.H.; Visualization, J.W.; Writing—original draft, J.W.; Writing—review and editing, J.W. and R.H. All authors have read and agreed to the published version of the manuscript.

Funding: This research was funded by the Advanced Manufacturing Office of the Office of Energy Efficiency and Renewable Energy of the U.S Department of Energy under award numbers DE-EE0008409 and DE-EE0009423.

Data Availability Statement: Not applicable.

Conflicts of Interest: The authors declare no conflict of interest.

Appendix A

Table A1. Single GFM IBR microgrid model parameters. System base: 2.5 MVA, 4160 V/480 V, 2 π 60 rad/s.

Param.	Value	Param.	Value	Param.	Value
Common Parameters					
S_b	2.5 MVA	V_b	480 V	ω_b	2 π60 rad/s
Y_b	10.85 S	Z_b	0.0922 Ω		
I1 GFM IBR Parameters, Base: 1.0 MVA, 480 V					
R_1	0.1 mΩ	L_1	30.0 µH	C_1	1.9 mF
R_2 *	0.0037 Ω	L_2 *	132.0 µH	k_{pi}	0.05 V/A
k_{ii}	2.5 V/As	k_{pv}	10.0 A/V	k_{iv}	1000.0 A/Vs
ω_{c1}	2500.0 rad/s	ω_{c2}	100.0 rad/s	d_p	0.01 pu
d_q	0.05 pu				
I2 GFL IBR Parameters, Base: 2.0 MVA, 480 V					
R_1	0.001 Ω	L_1	150.0 µH	C_1	1.3 mF
R_2 **	0.92 mΩ	L_2 **	35.4 µH	k_{pi}	0.1 V/A
k_{ii}	1.0 V/As	k_{pp}	100.0 A/MVA	k_{ip}	8000.0 A/MVAs
ω_{c1}	2500.0 rad/s	ω_{c2}	628.0 rad/s	k_{ppll}	10.0 rad/sV
k_{ipll}	1000.0 rad/s^2V				
G1 SG Parameters, Base: 2.5 MVA, 4160 V					
L_{ls}	0.01457 pu	R_s	0.007293 pu	L_{md}	1.7503 pu
L_{mq}	1.7503 pu	L_{lkd}	0.2898 pu	R_{kd}	0.0207 pu
L_{lfd}	0.1148 pu	R_{fd}	0.00058 pu	L_{lkq1}	0.1504 pu
R_{kq1}	0.1115 pu	L_{lkq2}	0.4407 pu	R_{kq2}	0.09327 pu
H	0.736 s	D	0.01 pu		
Network Parameters					
$R_{1,LN1}$	0.7157 Ω	$L_{1,LN1}$	1.661 mH	$R_{1,LN2}$	0.0837 Ω
$L_{1,LN2}$	0.276 mH	$R_{1,LD1}$	5.769 Ω		

* Referred to 480 V side of I1 step up transformer (see Figure 1) ; ** Referred to 480 V side of I2 step up transformer (see Figure 1).

Table A2. Multiple GFM IBR Microgrid model parameters. System base: 2.5 MVA, 4160 V/480 V, 2 π 60 rad/s.

Param.	Value	Param.	Value	Param.	Value
IBR1–IBR3 GFM IBR Parameters, Base: 1.0 MVA, 480 V					
R_1	0.001 Ω	L_1	30.0 µH	C_1	1.91 mF
R_2 *	0.0168 Ω	L_2 *	176.0 µH	k_{pi}	0.05 V/A
k_{ii}	2.5 V/As	k_{pv}	10.0 A/V	k_{iv}	$10e^3$ A/Vs
ω_{c1}	2500.0 rad/s	ω_{c2}	100.0 rad/s	d_p	0.02 pu
d_q	0.05 pu				
IBR4 GFL IBR Parameters, Base: 4.0 MVA, 480 V					
R_1	0.00538 Ω	L_1	400.0 µH	C_1	2.3 mF
R_2 **	0.415 mΩ	L_2 **	6.01 µH	k_{pi}	0.2 V/A
k_{ii}	3.26 V/As	k_{pp}	100.0 A/MVA	k_{ip}	$10e^3$ A/MVAs
ω_{c1}	2500.0 rad/s	ω_{c2}	100.0 rad/s	k_{ppll}	5.0 rad/sV
k_{ipll}	500.0 rad/s^2V				

Table A2. *Cont.*

Param.	Value	Param.	Value	Param.	Value
G1–G4 Diesel Generator Parameters ***, Base: 2.5 MVA, 13.8 kV					
K_p	15.0 pu	K_i	4.0 pu	d_p	0.02 pu
T_p	0.1 s	T_{act}	0.1 s	T_e	0.024 s
K_A	100.0 pu	T_A	0.02 s	K_F	0.03 pu
T_F	1.0 s	d_q	0.01 pu	T_v	0.001 s
T_{ex}	0.8 s	SE	0.12 pu	K_E	1.0 pu
K_C	0.3 pu	K_D	1.0 pu		

* Referred to 480 V sides of IBR1–IBR3 step up transformers (see Figure 2); ** Referred to 480 V side of IBR4 step up transformer (see Figure 2); *** See Table A1 for G1–G4 SG winding and mechanical parameters.

References

1. Hernandez-Alvidrez, J.; Darbali-Zamora, R.; Flicker, J.D.; Shirazi, M.; VanderMeer, J.; Thomson, W. Using Energy Storage-Based Grid Forming Inverters for Operational Reserve in Hybrid Diesel Microgrids. *Energies* **2022**, *15*, 2456. [CrossRef]
2. Jabeck, B. *The Impact of Generator Set Underloading*, LEXE0832-01. Deerfield: Caterpillar Inc. 2014. Available online: https://s7d2.scene7.com/is/content/Caterpillar/CM20151029-39727-00007?_ga=2.135155441.1302000910.1615573472-291789971.1615573472 (accessed on 1 August 2023).
3. Farrokhabadi, M.; Cañizares, C.A.; Simpson-Porco, J.W.; Nasr, E.; Fan, L.; Mendoza-Araya, P.A.; Tonkoski, R.; Tamrakar, U.; Hatziargyriou, N.; Lagos, D.; et al. Microgrid Stability Definitions, Analysis, and Examples. *IEEE Trans. Power Syst.* **2020**, *35*, 13–29. [CrossRef]
4. Fang, J.; Li, H.; Tang, Y.; Blaabjerg, F. On the Inertia of Future More-Electronic Power Systems. *IEEE J. Emerg. Sel. Top. Power Electron.* **2019**, *7*, 2130–2146. [CrossRef]
5. Lasseter, R.H.; Chen, Z.; Pattabiraman, D. Grid-Forming Inverters: A Critical Asset for the Power Grid. *IEEE J. Emerg. Sel. Top. Power Electron.* **2020**, *8*, 925–935. [CrossRef]
6. Lasseter, R.H.; Eto, J.H.; Schenkman, B.; Stevens, J.; Vollkommer, H.; Klapp, D.; Linton, E.; Hurtado, H.; Roy, J. CERTS Microgrid Laboratory Test Bed. *IEEE Trans. Power Deliv.* **2011**, *26*, 325–332. [CrossRef]
7. Lin, Q.; Uno, H.; Ogawa, K.; Kanekiyo, Y.; Shijo, T.; Arai, J.; Matsuda, T.; Yamashita, D.; Otani, K. Field Demonstration of Parallel Operation of Virtual Synchronous Controlled Grid-Forming Inverters and a Diesel Synchronous Generator in a Microgrid. *IEEE Access* **2022**, *10*, 39095–39107. [CrossRef]
8. Lopes, J.A.P.; Moreira, C.L.; Madureira, A.G. Defining control strategies for MicroGrids islanded operation. *IEEE Trans. Power Syst.* **2006**, *21*, 916–924. [CrossRef]
9. Pulcherio, M.C.; Renjit, A.A.; Illindala, M.S.; Khalsa, A.S.; Eto, J.H.; Klapp, D.A.; Lasseter, R.H. Evaluation of Control Methods to Prevent Collapse of a Mixed Source Microgrid. *IEEE Trans. Ind. Appl.* **2016**, *20*, 4566–4576. [CrossRef]
10. Mondal, A.; Illindala, M.S. Improved Frequency Regulation in an Islanded Mixed Source Microgrid through Coordinated Operation of DERs and Smart Loads. *IEEE Trans. Ind. Appl.* **2018**, *54*, 112–120. [CrossRef]
11. Du, W.; Lasseter, R.H.; Kalsa, A.S. Survivability of Autonomous Microgrid during Overload Events. *IEEE Trans. Smart Grid* **2019**, *10*, 3515–3524. [CrossRef]
12. Kenyon, R.W.; Sajadi, A.; Bossart, M.; Hoke, A.; Hodge, B. Interactive Power to Frequency Dynamics between Grid-Forming Inverters and Synchronous Generators in Power Electronics-Dominated Power Systems. *IEEE Syst. J.* **2023**, 1–12. [CrossRef]
13. Paquette, A.D.; Divan, D.M. Virtual Impedance Current Limiting for Inverters in Microgrids with Synchronous Generators. *IEEE Trans. Ind. Appl.* **2015**, *51*, 1630–1638. [CrossRef]
14. Pogaku, N.; Prodanovic, M.; Green, T.C. Modeling, Analysis and Testing of Autonomous Operation of an Inverter-Based Microgrid. *IEEE Trans. Power Electron.* **2007**, *22*, 613–625. [CrossRef]
15. Rasheduzzaman, M.; Mueller, J.A.; Kimball, J.W. An Accurate Small-Signal Model of Inverter-Dominated Islanded Microgrids Using dq Reference Frame. *IEEE J. Emerg. Sel. Top. Power Electron.* **2014**, *2*, 1070–1080. [CrossRef]
16. Qoria, T.; Gruson, F.; Colas, F.; Guillaud, X.; Debry, M.-S.; Prevost, T. Tuning of Cascaded Controllers for Robust Grid-Forming Voltage Source Converter. In Proceedings of the 20th Power System Computation Conference (PSCC), Dublin, Ireland, 11–15 June 2018.
17. Du, W.; Chen, Z.; Schneider, K.P.; Lasseter, R.H.; Pushpak Nandanoori, S.; Tuffner, F.K.; Kundu, S. A Comparative Study of Two Widely Used Grid-Forming Droop Controls on Microgrid Small-Signal Stability. *IEEE J. Emerg. Sel. Top. Power Electron.* **2020**, *8*, 963–975. [CrossRef]
18. Paquette, A.D.; Reno, M.J.; Harley, R.G.; Divan, D.M. Sharing Transient Loads: Causes of Unequal Transient Load Sharing in Islanded Microgrid Operation. *IEEE Ind. Appl. Mag.* **2014**, *20*, 23–34. [CrossRef]
19. Huang, L.; Xin, H.; Wang, Z.; Zhang, L.; Wu, K.; Hu, J. Transient Stability Analysis and Control Design of Droop-Controlled Voltage Source Converters Considering Current Limitation. *IEEE Trans. Smart Grid* **2019**, *10*, 578–591. [CrossRef]

20. Oureilidis, K.O.; Demoulias, C.S. A Fault Clearing Method in Converter-Dominated Microgrids with Conventional Protection Means. *IEEE Trans. Power Electron.* **2016**, *31*, 4628–4640. [CrossRef]
21. Tayyebi, A.; Dominic, G.; Adolfo, A.; Kupzog, F.; Dorfler, F. Frequency Stability of Synchronous Machines and Grid-Forming Power Converters. *IEEE J. Emerg. Sel. Top. Power Electron.* **2020**, *8*, 1004–1018. [CrossRef]
22. Sajadi, A.; Kenyon, R.W.; Hodge, B. Synchronization in Electric Power Networks with Inherent Heterogeneity up to 100% Inverter-Based Renewable Generation. *Nat. Commun.* **2022**, *13*, 2490. [CrossRef]
23. Naresh Kumar, V.; Parida, S.K. Modeling, Parameter Optimization of Universal Droop and Internal Model Controller for Multi Inverter-Fed DGs Based on Accurate Small-Signal Model. *IEEE Access* **2019**, *7*, 101928–101940. [CrossRef]
24. He, J.; Wu, X.; Wu, X.; Xu, Y.; Guerrero, J.M. Small-Signal Stability Analysis and Optimal Parameters Design of Microgrid Clusters. *IEEE Access* **2019**, *7*, 36896–36909. [CrossRef]
25. Miao, Z.; Domijan, A.; Fan, L. Investigation of Microgrids with Both Inverter Interfaced and Direct AC-Connected Distributed Energy Resources. *IEEE Trans. Power Deliv.* **2011**, *26*, 1634–1642. [CrossRef]
26. Malik, S.M.; Sun, Y.; Ai, X.; Chen, Z.; Wang, K. Small-Signal Analysis of a Hybrid Microgrid with High PV Penetration. *IEEE Access* **2019**, *7*, 119631–119643. [CrossRef]
27. Conte, F.; Massucco, S.; Silvestro, F.; Baccino, F.; Serra, P. Equivalent Modelling of Reciprocating Engines Generators for Microgrid Frequency Response Analysis. In Proceedings of the IEEE Manchester PowerTech Conference, Manchester, UK, 18–22 June 2017. [CrossRef]
28. Qoria, T.; Cossart, Q.; Li, C.; Guillaud, X.; Colas, F.; Gruson, F.; Kestelyn, X. Deliverable 3.2 Local Control and Simulation Tools for Large Transmission Systems, Horizon 2020-LCE-6. MIGRATE. 2018. Available online: https://www.h2020-migrate.eu/_Resources/Persistent/5c5beff0d5bef78799253aae9b19f50a9cb6eb9f/D3.2%20-%20Local%20control%20and%20simulation%20tools%20for%20large%20transmission%20systems.pdf (accessed on 1 August 2023).
29. Westman, J.; Hadidi, R. Influence of Power-Frequency Droop on Grid Forming Inverter Current Damping in Mixed Source Islanded Microgrids. In Proceedings of the 59th Industrial and Commercial Power Systems Technical Conference (I&CPS), Las Vegas, NV, USA, 21–25 May 2023. [CrossRef]
30. Krause, P.; Wasynczuk, O.; Sudhoff, S. *Analysis of Electric Machinery and Drive Systems*, 2nd ed.; John Wiley & Sons: Hoboken, NJ, USA, 2002; Chapter 5, pp. 200–205, ISBN 0-471-14326-X.
31. Salcedo, R.; Corbett, E.; Smith, C.; Limpaecher, E.; Rekha, R.; Nowocin, J.; Lauss, G.; Fonkwe, E.; Almeida, M.; Gartner, P.; et al. Banshee Distribution Network Benchmark and Prototyping Platform for Hardware-in-the-Loop Integration of Microgrid and Device Controllers. *IET J. Eng.* **2019**, *2019*, 5365–5373. [CrossRef]
32. PowerSystemHIL/EPHCC. Available online: https://github.com/PowerSystemsHIL/EPHCC/tree/master/DistributionSystems/SimulinkOpal/Banshee (accessed on 8 August 2023).
33. Roy, S.; Malik, O.P.; Hope, A.G. An Adaptive Control Scheme for Speed Control of Diesel Power-Plants. *IEEE Trans. Energy Conv.* **1991**, *6*, 605–611. [CrossRef]
34. Ponte, P. *Transient Performance of Generating Sets*; 5544421; Cummins Inc.: Columbus, IN, USA, 2019. Available online: https://mart.cummins.com/imagelibrary/data/assetfiles/0058629.pdf (accessed on 1 August 2023).
35. *Std 421.5-2016*; IEEE Recommended Practice for Excitation System Models for Power System Stability Studies. IEEE: Piscataway, NJ, USA, 2016.
36. Kundur, P. *Power System Stability and Control*; McGraw-Hill: New York, NY, USA, 1994; Chapter 12, pp. 715–716.
37. Zenelis, I.; Wang, X.; Kamwa, I. Online PMU-Based Wide-Area Damping Control for Multiple Inter-Area Modes. *IEEE Trans. Smart Grid* **2020**, *11*, 5451–5461. [CrossRef]
38. Shi, X.; Ruan, G.; Lu, H.; Chen, H.; Cai, W.; Ron, H.; Chen, G.; Zhao, Y. Analysis of Ultra-Low Frequency Oscillation in Hydro-Dominant Power System and Suppression Strategy by GPSS. *IEEE Trans. Ind. Appl.* **2023**, *59*, 2796–2806. [CrossRef]
39. *Std 1547-2018*; IEEE Standard for Interconnection and Interoperability of Distributed Energy Resources with Associated Electric Power Systems Interfaces. IEEE: Piscataway, NJ, USA, 2018.